nature communications

Article

https://doi.org/10.1038/s41467-026-70348-9

CAMPER: mechanistic artificial intelligence for designing peptides that target MRSA persisters

Received: 4 August 2025

Accepted: 19 February 2026

Published online: 09 March 2026

Check for updates

Fadi Shehadeh[1,2,10], Biswajit Mishra[1,3,10], Raquel Ferrer-Espada[4], Anindya Basu[5,6], LewisOscar Felix[1], Charilaos Dellis[1], Narchonai Ganesan[1], Liyang Zhang[1], Andrew T. Martens[4], Youlian Goulev[4], Michael B. Sherman[7], Johan Paulsson[4], Mandar T. Naik[8], Paul P. Sotiriadis[2,9] & Eleftherios Mylonakis[1,3]

Developing short, stable, and potent antimicrobial peptides is a promising strategy to combat antibiotic resistance and persistence. We present CAMPER (**C**onstraint-driven **AMP** **E**ngineering with **R**anking), a mechanistic artificial intelligence framework that integrates machine learning with biophysical ranking to prioritize membrane-targeting peptides effective against persister and biofilm forms of methicillin-resistant *Staphylococcus aureus*. We apply CAMPER to identify WP-CAMPER1 (12mer) that kills *S. aureus* MW2 at a minimal inhibitory concentration of 4 μg/mL. A 2% topical WP-CAMPER1 formulation reduces *S. aureus* MW2 burden by 2.5 $\log_{10}$ ($p < 0.0002$) in a murine prophylactic skin infection model, while its D-enantiomer, WP-CAMPER1-d, achieves 1.37 $\log_{10}$ ($p < 0.0001$) reduction in an established biofilm infection model. Single-cell analysis using a high-throughput microfluidic system shows that WP-CAMPER1-d reduces exponential-phase persisters of *S. aureus* USA300, and, in a deep-seated murine thigh infection model, decreases stationary-phase *S. aureus* MW2 persisters by 1.6 $\log_{10}$ ($p < 0.0001$).

The Centers for Disease Control and Prevention (CDC) identifies antimicrobial resistance (AMR) as an urgent global public health threat[1,2]. Annually, over 2.8 million antimicrobial-resistant infections occur in the United States, resulting in more than 35,000 deaths[1], with *Staphylococcus aureus* being a leading cause of severe healthcare-associated infections, including sepsis, pneumonia, endocarditis, and osteomyelitis[3]. The CDC estimates that methicillin-resistant *S. aureus* (MRSA) alone accounts for over 70,000 serious infections and nearly 9000 deaths each year[4], while vancomycin-resistant *S. aureus* (VRSA), even though it remains rare, is another emerging threat[5]. Further compounding the AMR challenge, *S. aureus* can transition into low-energy states, such as persisters[6], and form biofilms[7], adaptations that enable it to evade conventional antibiotic therapy and contribute to chronic and relapsing infections[8], underscoring the urgent need for alternative therapies.

Antimicrobial peptides (AMPs) represent a promising class of therapeutic agents capable of targeting drug-resistant bacteria and physiologically distinct forms such as persisters and biofilms,

[1]Department of Medicine, Houston Methodist Hospital, Houston, TX, USA. [2]Department of Electrical and Computer Engineering, National Technical University of Athens, Athens, Greece. [3]Department of Medicine, Weill Cornell Medical College, New York, NY, USA. [4]Department of Systems Biology, Blavatnik Institute, Harvard Medical School, Boston, MA, USA. [5]School of Pharmaceutical Sciences, Rajiv Gandhi Technological University, Bhopal, India. [6]School of Biomolecular Engineering & Biotechnology, Rajiv Gandhi Technological University, Bhopal, India. [7]Department of Biochemistry and Molecular Biology, Sealy Center for structural Biology and Molecular Biophysics, The University of Texas Medical Branch at Galveston, Galveston, TX, USA. [8]Department of Molecular Biology, Cell Biology and Biochemistry, Brown University, Providence, RI, USA. [9]Archimedes-Athena Research Center, Marousi, Greece. [10]These authors contributed equally: Fadi Shehadeh, Biswajit Mishra. e-mail: emylonakis@houstonmethodist.org

without promoting resistance[8,9]. Unlike conventional antibiotics, which primarily target active biosynthetic pathways in metabolically active bacterial cells[10], AMPs primarily disrupt the bacterial membranes[11], an appealing strategy against both persisters and biofilms, as membrane disruption occurs independently of the bacterial growth state[12]. Precisely designing AMPs for selective bacterial membrane disruption using traditional methods[13,14] relies on rational modifications to properties such as charge, hydrophobicity, helicity, and amphipathicity[11]. These approaches are often constrained by the time and resources required to explore complex sequence spaces. As an alternative, machine learning (ML) has emerged as a powerful tool for AMP discovery, enabling rapid candidate prediction by identifying patterns in sequence and physicochemical data[15–28].

ML-based approaches provide important statistical associations but overlook key mechanistic features, such as membrane selectivity and structural feasibility, limiting their biological relevance[15–28]. Several prior studies have incorporated physicochemical and structural features into ML classifiers, including hydrophobicity, net charge, and helix-forming propensity, as part of their feature sets[17,18,29]. While these approaches capture statistical associations between biophysical properties and activity, they treat these properties as input variables for supervised learning rather than as explicit mechanistic constraints. As a result, they overlook the biophysical requirements that define membrane-active AMP behavior, such as selective membrane interaction, amphipathic folding, and the structural feasibility of helical conformations.

To address this gap, we developed a Mechanistic Artificial Intelligence (AI) framework that integrates an ML model with a biophysically informed scoring function. We refer to our hybrid model as CAMPER (**C**onstraint-driven **AMP** **E**ngineering with **R**anking), reflecting its dual-stage approach: an ML classifier trained on experimental AMP data, and a biophysical scoring function that imposes mechanistic constraints. The ML component scores peptides based on key physicochemical properties required for membrane activity[11], effectively ranking candidates by both statistical likelihood and mechanistic plausibility. Our ML classifier, a random forest (RF) trained on chemical, structural, and sequence features, provides high-throughput probabilistic predictions of antimicrobial activity. The biophysical scoring function evaluates the potential of each peptide to function as a membrane-active AMP based on well-established biophysical properties: net charge, hydrophobicity, hydrophobic moment, and helicity[8,11,24].

We developed CAMPER to prioritize membrane-active AMPs with the specific aim of targeting drug-tolerant bacterial phenotypes such as biofilms and persister cells. We applied CAMPER to screen a mastoparan-derived peptide library and identified WP-CAMPER1 as the top candidate. In a proof-of-concept study, we evaluated WP-CAMPER1 across a series of in vitro and in vivo models, confirming its potent activity against the staphylococcal membrane, a property that strongly predicts efficacy against persisters[8,30]. Then, we confirmed its activity against drug-resistant *S. aureus*, including biofilms and persister populations. We developed the D-enantiomer of WP-CAMPER1, and tested it in the Mother Machine[31,32], a single-cell microfluidic assay used to evaluate activity against rare exponential-phase persisters, and confirmed its efficacy against rare exponential-phase persisters. The Mother Machine enables real-time tracking of individual bacteria under controlled conditions that simulate in vivo environments, including nutrient limitation and dynamic drug exposure[31]. Finally, we confirmed the anti-persister potency of WP-CAMPER1-d against stationary phase persisters in a well-established neutropenic murine deep-tissue thigh infection model, which is widely used to assess anti-persister therapeutics with translational relevance for systemic clinical applications[12,30,33].

Results

To advance the discovery of target-specific AMPs, we focused on membrane-active peptides against *S. aureus* and developed CAMPER as a dual-component in silico pipeline that combines an ML classifier trained on curated AMP sequences with a scoring function based on four biophysical constraints relevant to the membrane-disruptive activity of α-helical peptides: net charge, hydrophobicity, hydrophobic moment, and helicity (Fig. 1). We focused on α-helical peptides because they are structurally simple, synthetically accessible, and tunable, making them ideal candidates for rational design and optimization using computational pipelines like CAMPER.

Dataset assembly and feature engineering

We began by training an RF classifier to serve as the first component of the CAMPER pipeline, predicting the antimicrobial activity of peptides against *S. aureus*. To construct the ML model, we collected 3961 peptide sequences with MIC measurements against *S. aureus* from the Database of Antimicrobial Activity and Structure of Peptides (DBAASP). The database included 2280 sequences we labeled as active (MIC ≤ 32 μg/mL) and 1431 as inactive (MIC ≥ 64 μg/mL), excluding those with MIC values between these thresholds. After removing sequences containing non-standard amino acids, we retained a final dataset of 3660 unique peptide sequences.

To assess model performance on unseen data, we first created a stratified 80 to 20 random split of the dataset. The 20% portion served as a holdout set. The training set contained 2928 peptides, with 1674 active peptides (57.2%) and 1254 inactive peptides (42.8%). The holdout set contained 732 peptides, with 419 active peptides (57.2%) and 313 inactive peptides (42.8%). These proportions match the class distribution of the full dataset, which consisted of 2093 active peptides (57.2%) and 1567 inactive peptides (42.8%). Next, we generated a total of 66 physicochemical descriptors to characterize each peptide and train the model on properties that may influence antimicrobial activity (Table S1). Additionally, we computed the Morgan fingerprint (2048-bit, radius 4) to represent the substructural features of each peptide, resulting in a combined feature set of 2114 descriptors.

Model training, evaluation, and robustness

We assessed performance using the homology-aware 5-fold cross-validation procedure described in the "Methods" section. Based on the sensitivity analysis, we selected an 80% similarity threshold as the most stable and well-balanced cutoff for homology-aware evaluation (Fig. S1). We evaluated several combinations of feature representations and classifiers; specifically, sequence-derived n-grams, and ProtBERT embeddings paired with RF, XGBoost, and logistic regression. Across these combinations, models built on physicochemical descriptors consistently outperformed those trained on sequence-derived n-grams and ProtBERT embeddings, and RFs produced the strongest overall discrimination (Fig. 2A, B and Table S2). The corresponding confusion matrices for all feature–model combinations are shown in Fig. S2, which illustrates the distribution of correct and incorrect predictions under homology-aware cross-validation.

The RF model achieved an accuracy of 78% on the holdout set, with a precision of 79%, recall of 83%, F1 score of 81%, and AUC of 82%. Under the homology-aware 5-fold cross-validation scheme, the RF classifier showed lower overall discrimination than in the random split, with a mean cross-validated AUC of 70% (Fig. 2C). This decrease reflects the stricter evaluation created by grouping peptides with substantial sequence similarity into the same fold, which reduces the amount of overlapping sequence information across training and validation subsets. The confusion matrix shows the distribution of true positive, false positive, true negative, and false negative predictions in the holdout set (Fig. 2E). As shown in the calibration plot in Fig. S3, the RF classifier produces reasonably calibrated probability estimates,

with a Brier score of 0.156 indicating good overall alignment between predicted probabilities and observed frequencies.

To validate model reliability, we performed y-randomization, shuffling the activity labels in the training data while preserving the feature values. After 100 iterations, the randomized models achieved an average accuracy of 52%, significantly lower than the 78% accuracy of the original model, confirming that the observed performance is not due to random associations within the data.

We evaluated feature importance within the RF classifier by ranking features according to their mean impurity-based importance scores (Fig. 2F). GRAVY ranked highest, followed by MolLogP and BertzCT. Several BCUT2D descriptors, along with molar refractivity and the Kappa shape indices, also appeared among the top contributors. The hydrophobic moment was likewise ranked highly. Overall, the model relied most on descriptors related to hydrophobicity, charge distribution, polarizability, and amphipathic structure.

Biophysical scorer integration

To refine the selection of peptides predicted by the first component of CAMPER, we integrated a biophysical scoring function alongside the RF classifier to generate the final ranking. The biophysical scoring function was designed to prioritize α-helical, membrane-active peptides targeting *S. aureus* by ranking candidates based on four key physicochemical properties: net charge, hydrophobicity, hydrophobic moment, and helicity. Detailed rationale for property selection and the mathematical transformations applied are described in the "Methods" section, with hyperparameter and weights of the biophysical scorer provided in Supplementary Results.

We calculated performance metrics on the held-out test set. As noted above, peptides with MIC ≤ 32 μg/mL were labeled as active, and those with MIC ≥ 64 μg/mL as inactive, with peptides in the intermediate range excluded from evaluation. Compared to the standalone RF model, which achieved a precision of 81%, CAMPER (RF combined with Biophysical Scorer) improved precision to 86%, representing a 5 percentage point increase in correctly identifying true positives among predicted actives (Table S2). Notably, the number of false positives (defined as peptides predicted as active by the model but labeled as inactive based on their MIC) decreased substantially from 92 in the RF model to just 21 with CAMPER, representing a 77% reduction (Fig. 2E). This reduction aligns with the intended use of CAMPER as a prioritization framework that screens large, custom peptide libraries and aims to minimize synthesis and testing of non-active peptides. CAMPER shows lower recall and a lower AUC compared to the standalone RF model (Fig. 2C and Table S2), but this decrease in recall and AUC primarily reflects the prioritization introduced by the biophysical scoring function, which favors peptides consistent with an α-helical, membrane-disruptive mechanism rather than optimizing discrimination across all antimicrobial mechanisms. Analysis of peptides in the external evaluation set that were experimentally labeled as active in the dataset, predicted as active by the RF model, but deprioritized by CAMPER, showed that 70% (140/200) were not predominantly α-helical based on AlphaFold2 structure predictions. These peptides and their predicted secondary structure classes are provided in Supplementary Data 1.

To assess the biophysical characteristics of peptides prioritized by CAMPER, we selected the top 50 test set predictions ranked by (i) the RF classifier alone, (ii) the biophysical scoring function alone, and (iii) the combined CAMPER score. Compared to RF-only predictions, CAMPER-ranked peptides showed higher median helicity and hydrophobic moment with tighter distributions around values characteristic of α-helical, membrane-active peptides targeting Gram-positive bacteria (Fig. S4). Additionally, the integration of the biophysical scoring function within CAMPER led to improvements in prediction precision within specific regions of the biophysical feature space. For example, among peptides with hydropathy (GRAVY) between −1.19 and 0.26, the precision increased from 72% (RF-only) to 95% with the CAMPER dual-component model (Fig. 2G), and for the 0.20–0.40 helicity range, precision increased from 75% to 97% (Fig. 2H). Similar improvements in precision were observed in additional regions of the biophysical feature space. Precision gains were also observed across various grand average of hydropathy, charge and hydrophobic moment bins

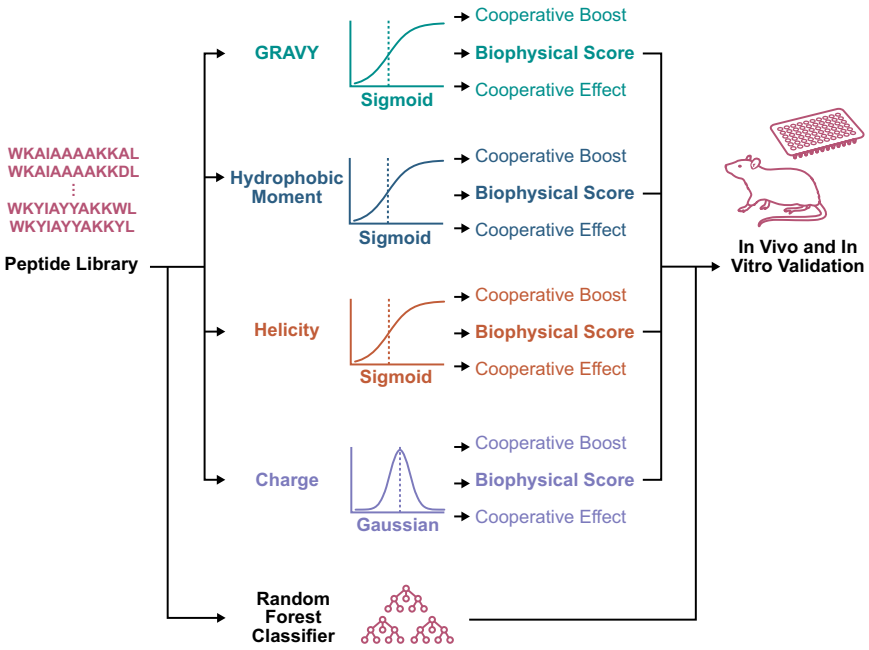

Fig. 1 | Overview of the CAMPER pipeline for antimicrobial peptide prioritization. Peptide sequences are first evaluated by an RF classifier trained to predict antimicrobial activity, producing a probability score for each sequence. The sequences are also independently assessed by a biophysical scoring module, which evaluates GRAVY, hydrophobic moment, helicity, and net charge. The RF probability and biophysical score are then combined to produce a final CAMPER score, which is used to prioritize candidates for in vitro and in vivo validation.

https://doi.org/10.1038/s41467-026-70348-9

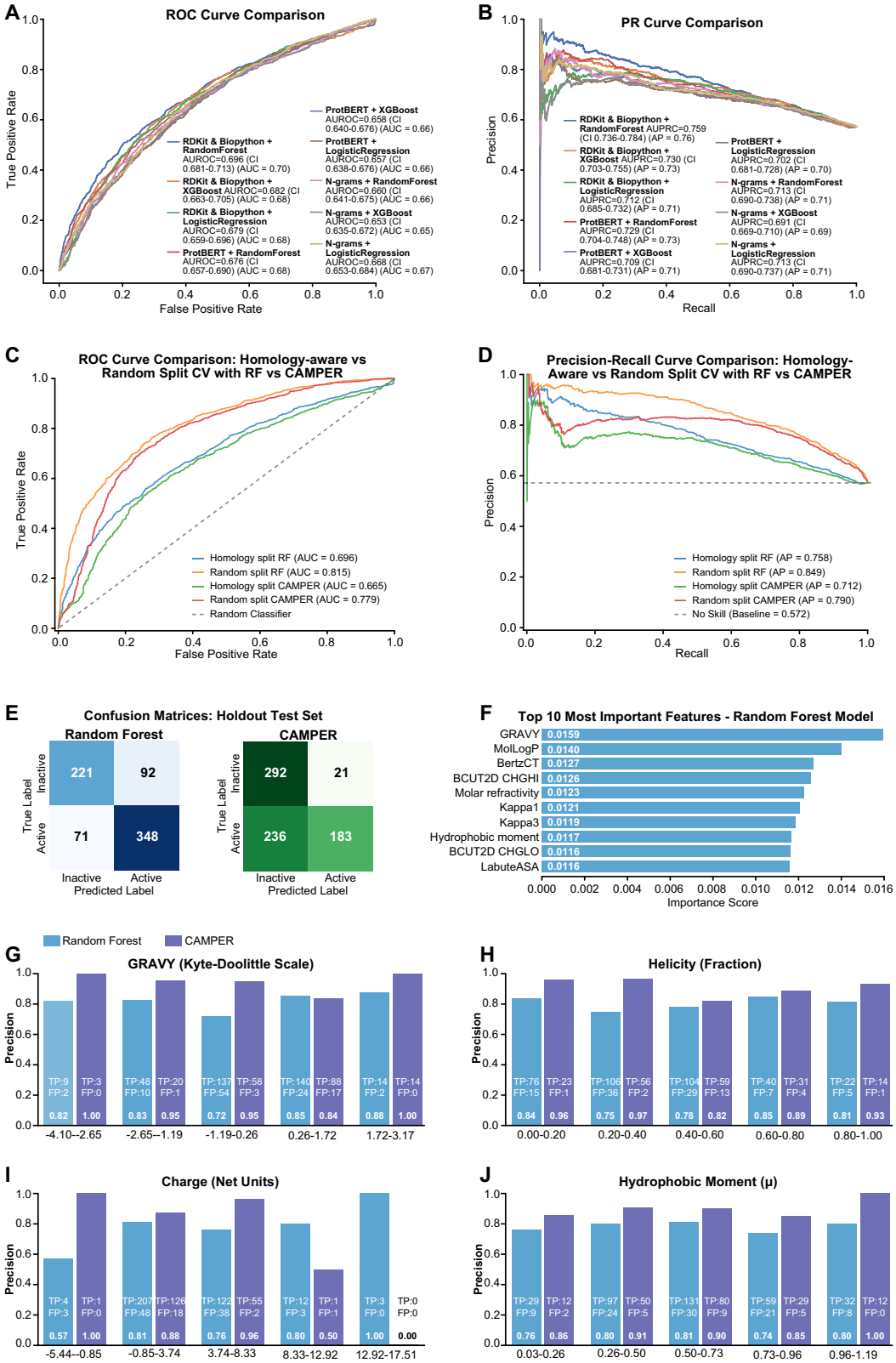

(Fig. 2G–I). At the same time, we observed a clear drop in precision in the highest charge interval, which includes only a small number of peptides and represents an extreme physicochemical regime that is not characteristic of most membrane-acting sequences (Fig. 2I). This pattern highlights that CAMPER performs best in well-represented and biologically relevant regions of the feature space while showing reduced precision in sparse, extreme outlier bins.

Application of CAMPER to a rationally designed peptide library

To demonstrate the ability of CAMPER to prioritize potent and membrane-active AMPs, we applied the pipeline to a candidate pool derived from a natural 14-mer peptide template, using it as a proof of concept for targeted in silico screening. Details on the peptide library generation are provided in the “Methods” section. We screened the peptide library with CAMPER and prioritized the five top-ranked

Fig. 2 | Classifier performance, homology-aware evaluation, feature importance, and CAMPER precision across the biophysical feature space. A Receiver operating characteristic (ROC) curve comparing all feature-model combinations; RDKit + Biopython descriptors, ProtBERT embeddings, and n-gram features for RF, XGBoost, and Logistic Regression classifiers, using homology-aware 5-fold cross-validation. **B** Precision–recall (PR) curves comparing all feature-model combinations; RDKit + Biopython descriptors, ProtBERT embeddings, and n-gram features for RF, XGBoost, and Logistic Regression classifiers, using homology-aware 5-fold cross-validation. **C** ROC comparison of RF and CAMPER under the homology-aware 5-fold cross-validation versus a stratified random 80/20 split. **D** PR comparison of RF and CAMPER under the homology-aware 5-fold cross-validation versus a stratified random 80/20 split. **E** Confusion matrices for the RF classifier and CAMPER on the 20% holdout test set, showing the distribution of true and predicted labels. **F** Top 10 most important features in the RF model, ranked by mean impurity-based importance scores. **G**–**J** Comparison of prediction precision between RF and CAMPER across binned values of GRAVY (**G**), helicity (**H**), charge (**I**), and hydrophobic moment (**J**).

Table 1 | Physical parameters of WP-CAMPER-designed peptides and their minimal inhibitory concentrations against *S. aureus* MW2

Peptide	Sequence[a]	NC[b]	Hy[c]	Hm[d]	Boman index[e]	rT[f] (min)	MIC (μg/mL) *SA*[g]
WP-CAMPER1	WKLIALLAKKLL	3	0.850	0.512	−1.56	18.925	4
WP-CAMPER2	WKWIALLAKKLL	3	0.896	0.509	−1.35	17.900	4
WP-CAMPER3	WKIIALLAKKLL	3	0.858	0.511	−1.56	19.575	4
WP-CAMPER4	WKLIAMIAKKLL	3	0.819	0.553	−1.35	15.808	4
WP-CAMPER5	WKVIALLAKKLL	3	0.810	0.519	−1.49	17.521	8
Van	N.A.	N.A.	N.A.	N.A.	N.A.	N.A.	1

[a]Peptide sequences have free N-terminus and is amidated at the C-terminus
[b]NC denotes net charge
[c]Hy:Hydrophobicity
[d]Hm:hydrophobic moment of respective peptides calculated from HeliQuest analysis (https://heliquest.ipmc.cnrs.fr/)
[e]Protein-binding potential (Boman index) in kcal/mol
[f]HPLC retention time (rT) in minutes on a C18 reverse-phase column
[g]Denotes *S. aureus* MW2

candidates for synthesis to enable rapid and efficient experimental assessment. WP-CAMPER1, the top-ranked candidate, exhibited a favorable physicochemical profile for membrane-targeting activity against Gram-positive bacteria with a GRAVY of 1.21, a hydrophobic moment of 0.538, a net charge of 2.55, and a helical propensity of 83.33%. The physicochemical profiles of all five synthesized candidates are summarized in Table 1.

In vitro antimicrobial potency of the top-ranked peptides

We evaluated the antimicrobial activity of WP-CAMPER1 followed by the next four top-ranked AMPs (WP-CAMPER2 to WP-CAMPER5), selected from the rationally designed peptide library described in the preceding section, using MIC assays against *S. aureus* strain MW2 (Table 1). WP-CAMPER1 exhibited a potent MIC of 4 μg/mL against *S. aureus* MW2. We also explored the antimicrobial robustness of the WP-CAMPER1 peptide by evaluating its antimicrobial activity under physiological salt conditions, varying pH levels, and in the presence of serum. The MIC of WP-CAMPER1 remained unchanged in the presence of monovalent and divalent salt (150 mM NaCl, 150 mM $MgSO_4$) and at pH levels of 7.4 and 8.0, except at pH 6.8, where it increased twofold. Similarly, the MIC increased only twofold in the presence of 5% human serum (Table S3).

Validation of WP-CAMPER1 by traditional quantitative-structure activity relationship (QSAR)-based peptide design

We conducted a QSAR analysis of WP-CAMPER1 to evaluate the hypothesis that CAMPER effectively ranks peptide sequences for membrane-disruptive antimicrobial activity by optimizing charge, hydrophobicity, and amphipathicity. In this series of analyses, we introduced substitutions of both hydrophilic and hydrophobic amino acids on different faces of WP-CAMPER1 (Fig. S5). We explored three conditions: increasing the charge, enhancing hydrophobicity, and altering both, as detailed in the "Methods" section.

The variants displayed MICs ranging from 4 to 8 μg/mL, depending on modifications to charge and hydrophobicity (Table S4). When only the charge or hydrophobicity was increased in WP-CAMPER1 (variants WP-CAMPER1-6K and WP-CAMPER1-5L8L), the antimicrobial potency was reduced, resulting in a higher MIC of 8 μg/mL. However, variants incorporating both increased charge and hydrophobicity (WP-CAMPER1-6K5L8L and WP-CAMPER1-6K3W5W7W11W) exhibited an MIC of 4 μg/mL against *S. aureus* MW2, comparable to that of WP-CAMPER1. These results indicate that further enhancement of charge or hydrophobicity does not improve activity, supporting the conclusion that CAMPER selected a sequence with physicochemical properties that are near-optimal for membrane-targeting antimicrobial efficacy.

Comparison of WP-CAMPER1 with other Mastoparan peptides

To demonstrate the utility of CAMPER in identifying peptides with enhanced antimicrobial potency, we synthesized three diverse mastoparan peptides (mastoparan-S, dominulin A, and mp_mastoparan) and evaluated their antimicrobial activity against *S. aureus* MW2, as well as their cytotoxicity in human liver-derived hepatocellular carcinoma (HepG2) cells and hemolysis of human red blood cells (Table S5). WP-CAMPER1 exhibited a MIC of 4 μg/mL against *S. aureus* MW2, while mastoparan-S (MIC = > 32 μg/mL), dominulin A (MIC = 32 μg/mL), and mp_mastoparan (MIC = 32 μg/mL), showed reduced antimicrobial potencies. WP-CAMPER1 had a lethal dose 50% (LD_{50}) of 128 μg/mL in HepG2 cells and caused 50% hemolysis at 64 μg/mL, whereas the mastoparans showed no toxicity to HepG2 cells (over 99% survival at 128 μg/mL) (Fig. S6A) and <40%, <20%, and <10% hemolysis for dominulin A, mp_mastoparans, and mastoparan-S, respectively, at 128 μg/mL (Fig. S6B). Although these peptides exhibit lower cytotoxicity, they show minimal or no antimicrobial activity against *S. aureus* MW2, limiting their relevance to CAMPER design goals and translational aims. In contrast, CAMPER enabled the design of WP-CAMPER1 from the same mastoparan scaffold, resulting in markedly superior antimicrobial potency, highlighting the utility of CAMPER in AMP design.

https://doi.org/10.1038/s41467-026-70348-9

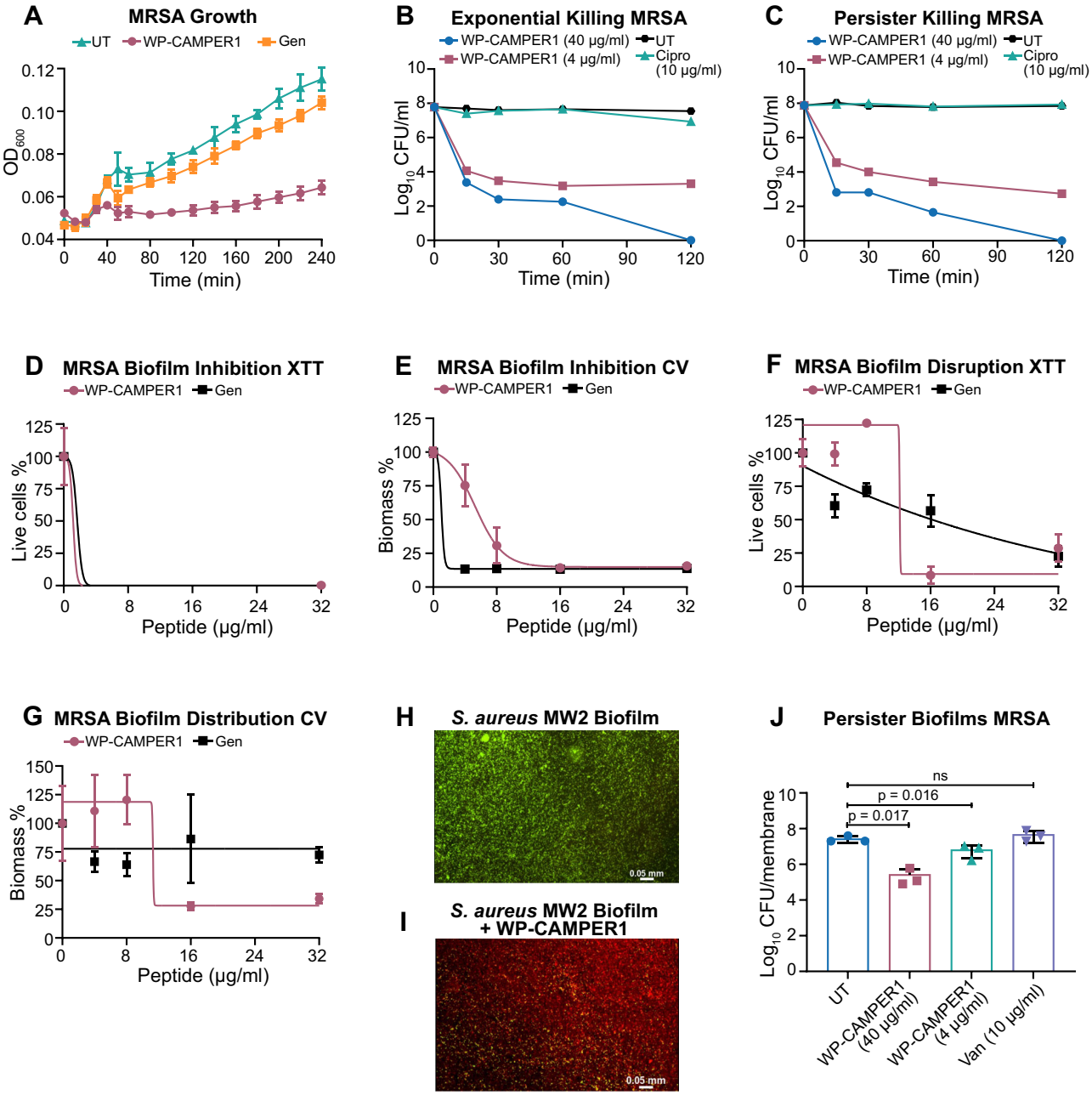

Fig. 3 | In vitro growth-inhibitory and bactericidal activity of WP-CAMPER1 against exponential, persister, and biofilm-associated *S. aureus* MW2. A Growth curve of *S. aureus* MW2 in the presence of WP-CAMPER1 and gentamicin (gen) at 32 μg/mL. Each group included three biologically independent replicates ($n = 3$), with data presented as mean ± standard deviation (SD). **B**, **C** Bactericidal kill kinetics of WP-CAMPER1 against *S. aureus* MW2 in exponential (**B**), and gentamicin-induced stationary persister states (**C**) at 4 and 40 μg/mL, compared to untreated bacterial control (UT). Ciprofloxacin (10 μg/mL) was included as an antibiotic control. CFU counts were measured over 120 min with data presented as mean for two biologically independent replicates. **D**, **E** Inhibition of *S. aureus* MW2 biofilm formation by WP-CAMPER1 (4–32 μg/mL), evaluated after 24 h using metabolic activity reduction (XTT assay) (**D**), and biomass quantification (crystal violet staining) (**E**). **F**, **G** Disruption of 24-h established *S. aureus* MW2 biofilms by WP-CAMPER1 (4–32 μg/mL), measured by reduction in live-cell viability (XTT assay) (**F**), and decrease in biomass (crystal violet staining) (**G**). Data in **D**–**G** are presented as mean ± SD from three ($n = 3$) biologically independent replicates. **H**, **I** Fluorescence microscopy images of 24-h *S. aureus* MW2 biofilms stained with live/dead stain: untreated control (**H**), and WP-CAMPER1 treated biofilms at 32 μg/mL (**I**). Scale bars: 0.05 mm. Images shown are representative of at least three independent experiments with similar results. **J** Disruption of 24-h established biofilms of *S. aureus* MW2 by WP-CAMPER1 at 4 and 40 μg/mL, assessed by log reduction in bacterial loads on solid membranes. Each group included three biologically independent replicates ($n = 3$), with data presented as mean ± SD. Statistical significance was determined by comparing two groups using an unpaired (two-tailed) Student's *t*-test. *p* values are indicated in the graph. Vancomycin (10 μg/mL) was included as an antibiotic control. Source data are provided as a Source data file.

Potency of WP-CAMPER1 towards drug-resistant *S. aureus* exponential and stationary phase persister cells

To confirm the membrane-targeting and antimicrobial potential of WP-CAMPER1, we first assessed its ability to inhibit the growth of exponential-phase *S. aureus* strains MW2 and VRS1, before testing its efficacy against more resilient forms such as biofilms and persisters. WP-CAMPER1 rapidly suppressed the growth of exponentially growing *S. aureus* MW2 bacterial cells compared to control antibiotics such as gentamicin and vancomycin (Figs. 3A, S7A, and S8A). Whereas vancomycin was not active against *S. aureus* VRS1 (Fig. S9A).

Subsequently, in time-kill kinetics assays, WP-CAMPER1 (40 μg/mL) eliminated 1×10^8 CFU of exponential and stationary phase persister cells of *S. aureus* MW2 within 120 min of exposure (Fig. 3B, C). We observed a similar result of complete cell killing within 120 min for 1×10^6 CFU of exponential and stationary phase persister cells of *S. aureus* VRS1 (Fig. S7B, C). WP-CAMPER1 (4 μg/mL) reduced *S. aureus* MW2 exponential and stationary phase persister bacterial counts by 3.2 $\log_{10}$ and 3.5 $\log_{10}$, respectively (Fig. 3B, C). Under the same conditions, the control antibiotic ciprofloxacin (at 10 μg/mL) reduced *S. aureus* MW2 exponential cells by only 0.5 $\log_{10}$ and showed no activity against stationary phase persister cells, confirming the presence of a drug-tolerant persister state (Fig. 3B, C). Similarly, WP-CAMPER1 (4 μg/mL) reduced *S. aureus* VRS1 exponential and stationary phase persister cell counts by approximately 2 $\log_{10}$ and 1.2 $\log_{10}$, respectively (Fig. S7B, C). The control antibiotic linezolid (at 100 μg/mL) reduced *S. aureus* VRS1 exponential cells by 1.0 $\log_{10}$ but was inactive against the persister form of *S. aureus* VRS1 (Fig. S7B, C). Bithionol was active against both exponential and persister populations of *S. aureus* MW2 and *S. aureus* VRS1 (Figs. S8B, C and S9B, C). Compared with untreated controls, bithionol reduced the exponential-phase bacterial load by approximately 3.0 $\log_{10}$ CFU in *S. aureus* MW2 and 1.5 $\log_{10}$ CFU in *S. aureus* VRS1 (Figs. S8B and S9B). In persister assays, bithionol decreased the bacterial burden by approximately 2.0 $\log_{10}$ CFU in *S. aureus* MW2 and 0.5 $\log_{10}$ CFU in *S. aureus* VRS1 (Figs. S8C and S9C).

Anti-biofilm activity of WP-CAMPER1 against drug-resistant *S. aureus* biofilms

Next, we tested the antibiofilm activity of WP-CAMPER1 against *S. aureus* MW2 and VRS1 biofilms by evaluating both biofilm inhibition (Figs. 3D, E and S7D, E) and disruption stages (Figs. 3F, G and S7F, G). WP-CAMPER1 inhibited biofilm formation by *S. aureus* MW2 and VRS1, inhibited 50% of *S. aureus* MW2 live cells at 2 μg/mL, and reduced biofilm biomass by 50% at 6 μg/mL ($MBIC_{50}$) (Fig. 3D, E). For *S. aureus* strain VRS1, WP-CAMPER1 achieved 50% killing of live cells at 6 μg/mL and a 50% reduction in biofilm mass at 4 μg/mL ($MBIC_{50}$) (Fig. S7D, E). Additionally, WP-CAMPER1 disrupted 24-h pre-established biofilm, killed 50% of live *S. aureus* MW2 biofilm cells, and reduced biofilm biomass by 50% ($MBEC_{50}$) at 12 μg/mL (Fig. 3F, G). For *S. aureus* VRS1, WP-CAMPER1 killed 50% of biofilm-embedded cells at 16 μg/mL and reduced biofilm biomass by 50% ($MBEC_{50}$) at 12 μg/mL (Fig. S7F, G).

To further evaluate the antibiofilm activity of WP-CAMPER1, we included three additional *S. aureus* clinical isolates (BF1, BF2, and BF3) (Fig. S10). WP-CAMPER1 effectively disrupted 24-h mature biofilms formed by these isolates, achieving 50% biomass reduction ($MBEC_{50}$) at 8 μg/mL, 16 μg/mL, and 12 μg/mL, respectively. Similarly, WP-CAMPER1 inhibited biofilm formation in these clinical isolates, reducing biomass by 50% ($MBIC_{50}$) at 1 μg/mL (BF1), 5 μg/mL (BF2), and 3 μg/mL (BF3). These results highlight the broad-spectrum antibiofilm efficacy of WP-CAMPER1 across diverse clinical *S. aureus* backgrounds.

To visually assess the antibiofilm potential of WP-CAMPER1, we performed fluorescence imaging on 24-h established *S. aureus* MW2 and VRS1 biofilms treated with WP-CAMPER1 (Figs. 3H, I and S7H, I). Untreated control biofilms displayed predominantly SYTO9 green fluorescence (Figs. 3H and S7H), indicating the presence of mostly live cells. In contrast, biofilms treated with WP-CAMPER1 (32 μg/mL) showed a pronounced propidium iodide red fluorescence, suggesting most cells were dead (Figs. 3I and S7I).

We then evaluated the ability of WP-CAMPER1 to disrupt 24-h established *S. aureus* MW2 and VRS1 biofilms grown on solid membrane supports (Figs. 3J and S7J). WP-CAMPER1 (40 μg/mL) reduced the bacterial burden in *S. aureus* MW2 biofilms by 2 $\log_{10}$ ($p = 0.017$) and in *S. aureus* VRS1 biofilms by 2.2 $\log_{10}$ ($p = 0.016$) (Figs. 3J and S7J), compared to the untreated control. At 4 μg/mL, WP-CAMPER1 lowered the bacterial burden by 0.3 $\log_{10}$ ($p = 0.016$) for *S. aureus* MW2 and 1.0 $\log_{10}$ ($p = 0.024$) for *S. aureus* VRS1 compared to the untreated control. In contrast, vancomycin at 10 μg/mL did not reduce bacterial burden in *S. aureus* MW2 or VRS1 strains.

Confirmation of membrane targeting

Because the biophysical scoring function was designed to prioritize peptides with physicochemical properties associated with membrane activity, it was essential to experimentally confirm that WP-CAMPER1, the top-ranked peptide, exerts its antimicrobial effect through direct interaction with the bacterial membrane. To this end, we conducted a series of peptide-membrane interaction studies.

To evaluate the initial membrane interaction and structural conformation of WP-CAMPER1 in a bacterial membrane-mimetic environment, we conducted circular dichroism (CD) spectroscopy in the presence of sodium dodecyl sulfate (SDS) micelles. The CD spectra exhibited characteristic minima at 208 and 222 nm, indicative of an α-helical conformation (Fig. S11). Furthermore, 2D NMR spectroscopy in the presence of SDS micelles revealed that WP-CAMPER1 adopted an α-helical structure with a distinct hydrophobic surface essential for membrane interaction (Fig. 4A–D). Extended structural calculations on the NMR structural restraints, hydrogen bonds, and Ramachandran plot statistics are provided in the Table S6 and Supplementary Results.

Molecular dynamics (MD) simulations demonstrated that WP-CAMPER1 bound to and disrupted a DOPC/DOPG(7:3) model membrane, with key residues tryptophan 1 and lysine 2, 9, and 10 forming stable hydrogen bonds and perturbing membrane integrity (Fig. 4E–H). Table S7 and Supplementary Results provide details of the simulation outcomes, including hydrogen bond occupancies between DOPG/DOPC and interacting amino acids, as well as membrane water perturbation following WP-CAMPER1 insertion.

To determine whether WP-CAMPER1 could disrupt a membrane model that more closely mimics the *S. aureus* lipid composition, we performed MD simulations of WP-CAMPER1 with a POPG:CL (7:3) bilayer. WP-CAMPER1 rapidly associated with the membrane, binding within the first 10 ns and remaining embedded throughout the 500-ns simulation, indicating a stable and energetically favorable peptide-membrane interaction (Fig. S12A). The partial density profile further demonstrated peptide insertion into the bilayer (Fig. S12B).

In the next series of studies, we aimed to confirm that the membrane binding and insertion behavior of WP-CAMPER1 observed in silico reflects true membrane-targeting activity by conducting biochemical assays to assess its effects on live *S. aureus* MW2 cells (Fig. 4I–R). Using a DiBAC4(3) fluorescence-based dye assay, we observed that WP-CAMPER1 (32 μg/mL) caused a rapid increase in fluorescence, signifying membrane depolarization (Fig. 4I). Similarly, a Triton X-100 (1% *v*/*v*) control depolarized most cells, displaying maximum fluorescence intensity. Untreated bacterial cells displayed no change in DiBAC4(3) fluorescence, indicating an intact membrane potential.

As an additional test to confirm whether WP-CAMPER1 can permeabilize membranes, we performed dye permeation experiments using propidium iodide and SYTOX Green. Upon co-incubation of *S. aureus* MW2 cells with WP-CAMPER1 (at 4 μg/mL) and propidium iodide, we detected elevated fluorescence, suggesting WP-CAMPER1-induced membrane damage (Fig. 4J). Similarly, WP-CAMPER1 (at 4 μg/mL) resulted in increased SYTOX Green fluorescence, further confirming membrane disruption (Fig. 4K). Additionally, WP-CAMPER1 at 4 μg/mL led to higher ATP luminescence levels compared with untreated controls, suggesting ATP leakage due to compromised membrane integrity (Fig. 4l).

To further establish the putative membrane-targeting nature of WP-CAMPER1, we employed a *ΔfmtC* transposon mutant from the Nebraska Transposon Mutant Library (NTML). This mutant lacks the ability to transfer a lysyl group onto the bacterial membrane surface[34], increasing its susceptibility to membrane-targeting antimicrobial

https://doi.org/10.1038/s41467-026-70348-9

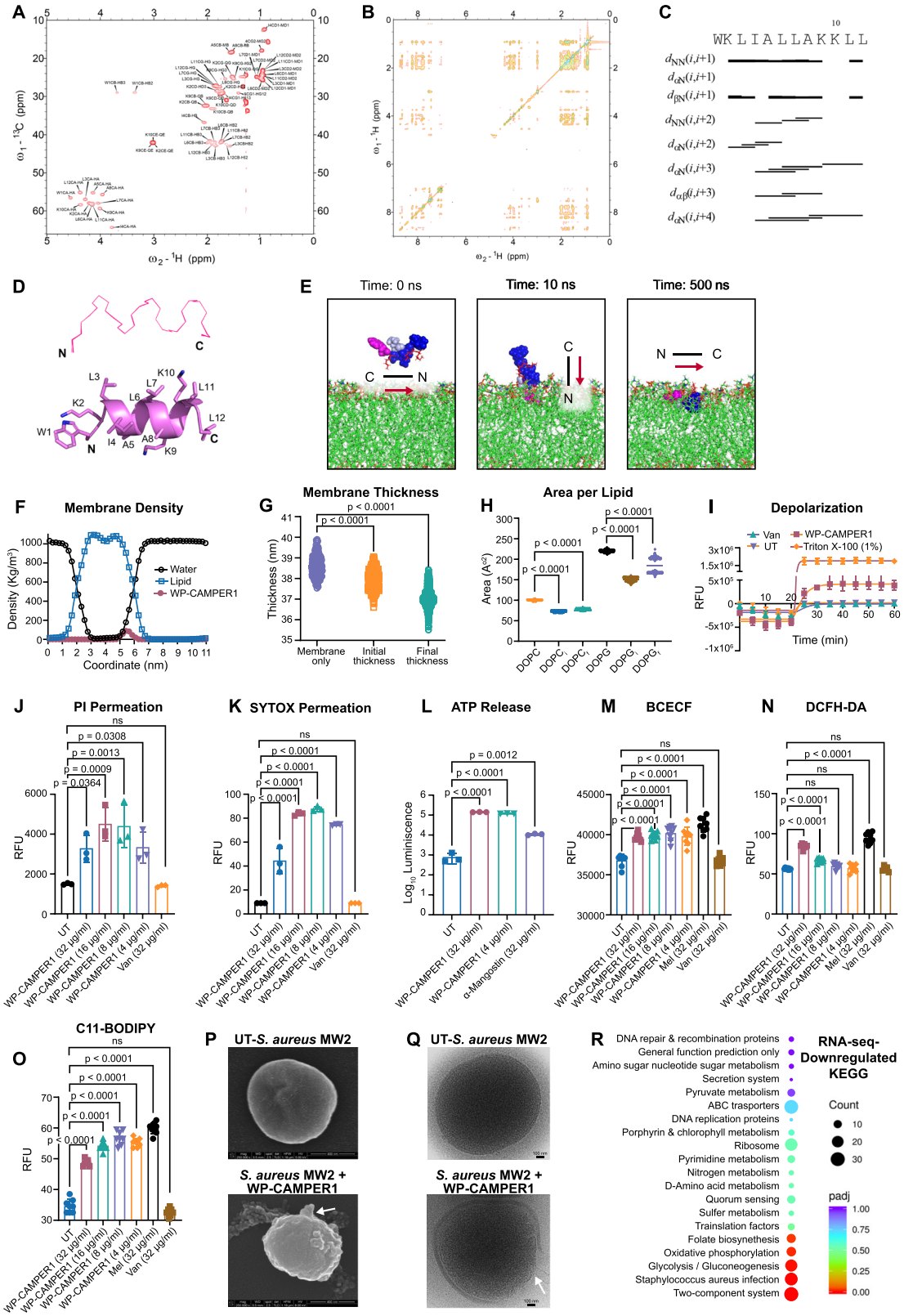

agents. Compared with the wild-type background JE2 strain, WP-CAMPER1 demonstrated a two-fold reduction in MIC against the *ΔfmtC* mutant, suggesting enhanced membrane-disruptive activity, likely due to the reduced positive charge from the absence of lysyl transfer (Table S8).

Next, to assess the membrane-associated physiological disruptions of live *S. aureus* MW2 cells, we used the fluorescent probe 2′,7′-Bis-(2-carboxyethyl)−5-(and-6)-carboxyfluorescein (BCECF) to monitor changes in the ΔpH component of the proton motive force (PMF). WP-CAMPER1 at 4 μg/mL significantly perturbed ΔpH levels (Fig. 4M). Additionally, WP-CAMPER1 (32 μg/mL) induced a marked increase in intracellular reactive oxygen species (ROS), as evidenced by enhanced fluorescence from the ROS-sensitive 2′,7′-Dichlorodihydrofluorescein diacetate dye (DCFH-DA) (Fig. 4N).

Fig. 4 | Structural and biophysical insights into membrane targeting by WP-CAMPER1. **A** Natural abundance 2D-^{13}C-HSQC, **B** 2D-NOESY spectrum, and **C** Summary of key NOE-derived distance restraints used for structural determination of WP-CAMPER1. **D** NMR-derived ensemble of WP-CAMPER1 solution structures (upper panel) and ribbon representation (lower panel). **E** Representative snapshot from all-atom MD simulation of WP-CAMPER1 into a DOPC:DOPG (7:3) bilayer at 500 ns. **F** Lipid density changes and membrane perturbation induced by WP-CAMPER1-mediated water intrusion. **G** Alterations in membrane thickness upon WP-CAMPER1 interaction. **H** Increase in average lipid surface area per molecule ($n = 200$ frames, represented as mean ± SD) following WP-CAMPER1 binding to the DOPC:DOPG (7:3) bilayer. **I** Membrane depolarization in *S. aureus* MW2 induced by WP-CAMPER1 (32 μg/mL). **J**, **K** Evaluation of membrane permeabilization by WP-CAMPER1, in comparison to untreated control (UT) and vancomycin (Van), using propidium iodide (PI) staining (**J**) and SYTOX Green staining (**K**). **L** Quantification of ATP release from *S. aureus* MW2 following exposure to WP-CAMPER1. **M** Intracellular pH perturbation in *S. aureus* MW2 following WP-CAMPER1 treatment. **N** Induction of intracellular ROS in *S. aureus* MW2 by WP-CAMPER1. **O** Induction of lipid peroxidation in *S. aureus* MW2 membranes by WP-CAMPER1. Data in **I**–**L** and **M**–**O** are presented as mean ± SD from three ($n = 3$) and eight ($n = 8$) biologically independent replicates, respectively. **P** SEM image of untreated *S. aureus* MW2 showing intact surface morphology (upper panel) and image of *S. aureus* MW2 treated with WP-CAMPER1 (bottom panel), showing membrane blebbing (white arrow). **Q** Cryo-EM image of untreated *S. aureus* MW2 with intact cellular ultrastructure (upper panel) and treated with WP-CAMPER1 (bottom panel), showing membrane perturbation (white arrow). For **P**, **Q**, images shown are representative of at least three independent experiments with similar results. **R** KEGG pathway enrichment analysis of downregulated genes in *S. aureus* MW2 following treatment with WP-CAMPER1 obtained from two biologically independent replicates, calculated using DESeq2[112]. For **G**, **H**, **I**–**O**, statistical significance was determined using two-sided one-way ANOVA followed by Dunnett's multiple-comparisons test, and p values are indicated in the graph. Source data file provided.

To determine whether ROS generation directly contributed to bacterial killing as an auxiliary mechanism in addition to peptide-induced membrane disruption, we performed kinetic growth and spot-titer CFU assays in the presence of the ROS scavenger *N*-acetylcysteine (NAC, 10 mM). In the kinetic growth assay, cultures with an initial inoculum of 1×10^6 CFU/mL showed a significant bacterial growth difference at 16 h when co-incubated with WP-CAMPER1 (1× MIC) and NAC ($p = 0.046$), whereas no growth recovery was observed in cultures treated with WP-CAMPER1 compared to untreated controls ($p = 0.011$) and NAC alone did not affect *S. aureus* MW2 growth (Fig. S13A). In the spot-titer CFU assay, NAC partially restored *S. aureus* MW2 viability, reducing the bactericidal effect of WP-CAMPER1 by approximately 5 $\log_{10}$ CFU after 4 h of co-incubation ($p = 0.0006$), compared with the untreated control that reached 8 $\log_{10}$ CFU (Fig. S13B). Similarly, using a higher inoculum (1×10^7 CFU/mL) treated with 5× MIC of WP-CAMPER1, initial bacterial killing was followed by partial regrowth in the presence of NAC, whereas complete eradication occurred with peptide treatment alone after 18 h (Fig. S13C). Together, these findings suggest that, in addition to direct membrane disruption, ROS generation contributed to the overall bactericidal mechanism of the CAMPER peptides.

To determine whether this oxidative stress led to lipid peroxidation, we employed a fluorescent-based assay using C11-BODIPY dye. WP-CAMPER1 (4 μg/mL) treatment significantly increased C11-BODIPY oxidation, indicating lipid peroxidation and ROS-mediated membrane damage (Fig. 4O).

Microscopic visualization of WP-CAMPER1-induced *S. aureus* membrane disruption

In order to visually confirm WP-CAMPER1-induced bacterial membrane damage, we employed scanning and cryo-transmission electron microscopy to examine *S. aureus* MW2 cells treated with the peptide WP-CAMPER1 at 40 μg/mL (Fig. 4P). Untreated bacterial control cells displayed smooth and uniform surfaces, indicating intact cells (Fig. 4P, upper panel). In contrast, WP-CAMPER1-treated cells exhibited prominent membrane blebbing, invaginations, and structural damage, indicating damage to bacterial membrane integrity caused by WP-CAMPER1 (Fig. 4P, bottom panel). We also performed cryo-transmission electron microscopy (cryo-TEM) on *S. aureus* MW2 cells treated with WP-CAMPER1 (80 μg/mL) to visualize ultrastructural changes in the bacterial membrane. Compared to the control cells (Fig. 4Q, upper panel), which displayed a homogeneous and intact membrane surface, WP-CAMPER1-treated cells exhibited membrane disruption, including invaginations, vacuole-like structures, and shrunken cytoplasm near the cell periphery (Fig. 4Q, bottom panel), suggesting compromised membrane integrity.

Transcriptional effect of WP-CAMPER1

We performed RNA-seq analysis on WP-CAMPER1-treated *S. aureus* to help elucidate the mechanism by which WP-CAMPER1 impacts bacterial membranes and thus affects *S. aureus* persisters and biofilms. We found that treatment with WP-CAMPER1 (2 μg/mL) significantly altered gene expression, causing 852 upregulated and 843 downregulated genes ($p < 0.05$) (Supplementary Data 2 and 3). Notably, WP-CAMPER1 significantly affected the expression of *S. aureus* pathways involved in bacterial virulence, oxidative phosphorylation, folate biosynthesis, and energy metabolism (Fig. 4R). These transcriptional changes reflect bacterial stress responses to WP-CAMPER1 and support our hypothesis that CAMPER-designed peptides selectively disrupt membrane integrity while triggering broader physiological effects. Detailed analysis of gene expression changes across multiple regulatory pathways is provided in the Supplementary Results.

In vivo therapeutic efficacy of WP-CAMPER1 on a murine skin infection model

To evaluate whether the bacterial membrane-targeting activity of WP-CAMPER1 translates into protective efficacy in vivo, we next tested its ability to reduce bacterial burden in a skin infection model that mimics early-stage or prophylactic intervention. We employed an abraded murine skin infection model, infecting mice with 10^7 CFU of *S. aureus* MW2 to evaluate the in vivo efficacy of WP-CAMPER1 (Fig. 5A). A single application of the 2% (*w*/*w*) WP-CAMPER1 formulation, administered 10 min after infection (representing a prophylactic model), led to a significant reduction in *S. aureus* MW2 bacterial load (evaluated after 24 h), achieving a 2.5 $\log_{10}$ decrease ($p = 0.0002$) (95% CI = 2.15–2.85) compared to the vehicle treated mice groups (Fig. 5B). The 1% (*w*/*w*) formulation also demonstrated efficacy, reducing the bacterial load by 1.4 $\log_{10}$ ($p = 0.0005$) (95% CI = 0.84–1.42). As a positive control, mupirocin ointment (2% *w*/*w*) resulted in a 2.2 $\log_{10}$ reduction in *S. aureus* MW2 burden ($p = 0.0002$) (95% CI = 1.82–2.48) compared to the vehicle-treated mice. In addition to decreased bacterial burden, the skin of mice treated with the WP-CAMPER1 (2% *w*/*w*) formulation exhibited significantly lower levels of proinflammatory cytokines and chemokines compared to the vehicle treated skin, including TNF-α (14-fold reduction, $p = 0.029$), IL-1β (4-fold, $p = 0.028$), IFN-γ (2.2-fold, $p = 0.004$), MCP-1 (2-fold, $p = 0.023$), and IL-6 (5-fold, $p = 0.002$) (Fig. S14).

Class A peptidomimetics of WP-CAMPER1

After confirming the membrane-targeting mechanism, in vitro potency, and topical efficacy of WP-CAMPER1, we sought to explore its efficacy in a murine thigh infection model of persistent *S. aureus*, which involves systemic administration of the study agent. Because WP-CAMPER1, like other α-helical peptides, could be vulnerable to

https://doi.org/10.1038/s41467-026-70348-9

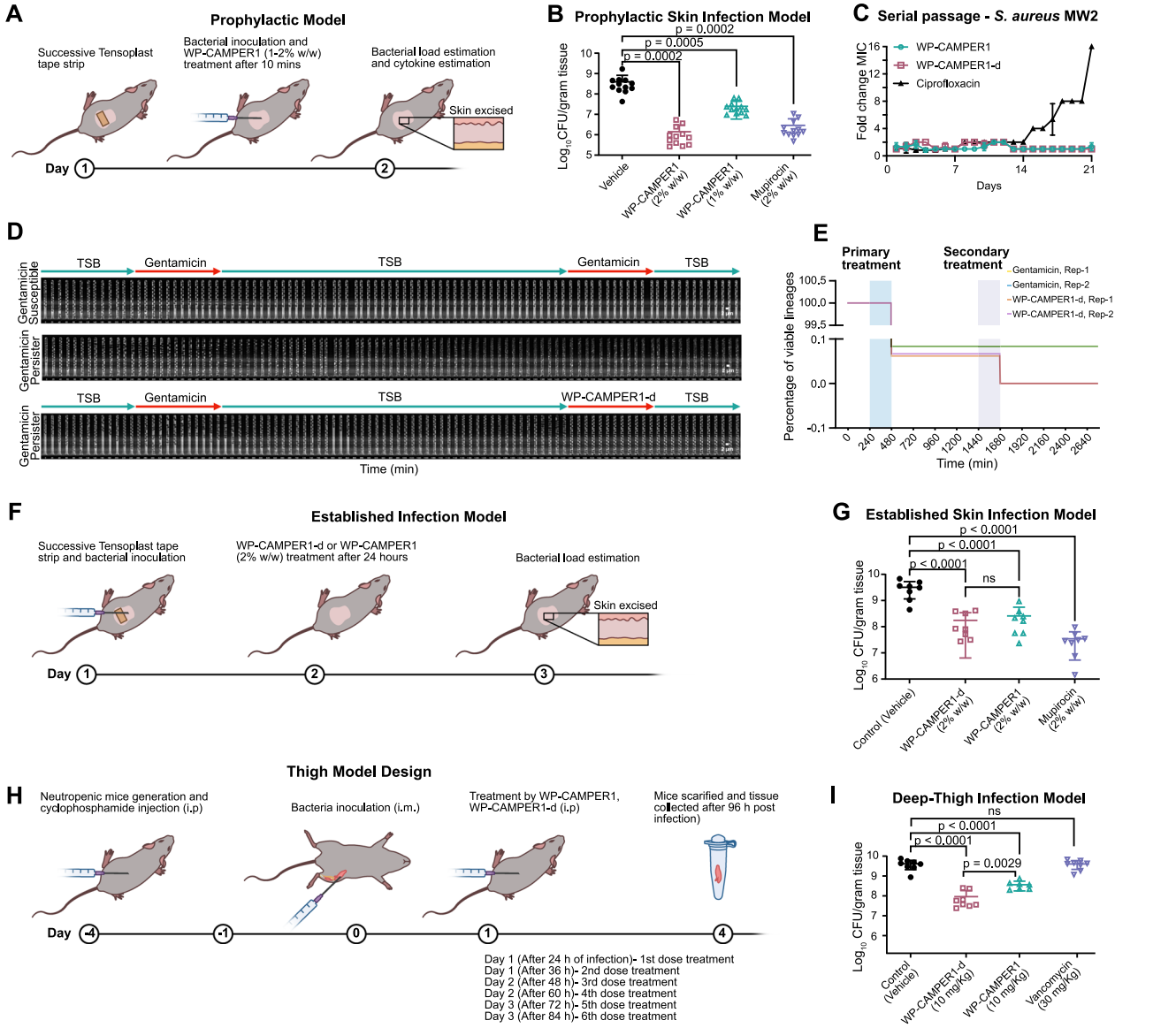

Fig. 5 | In vivo and microfluidic evaluation of WP-CAMPER1 and WP-CAMPER1-d against *S. aureus* MW2 in murine skin, single-channel-based microfluidics, and deep thigh infection models. A Schematic overview of the prophylactic skin-abraded murine infection model. **B** Quantification of bacterial burden in skin tissues from mice infected with exponential-phase *S. aureus* MW2 and treated 10 min post infection with WP-CAMPER1 (1% and 2% *w*/*w*), or mupirocin (2% *w*/*w*). Data represent mean ± SD of $n = 12$ biologically independent replicates. **C** Evaluation of resistance induction in *S. aureus* MW2 by WP-CAMPER1 and WP-CAMPER1-d. Data are presented as mean ± SD from three ($n = 3$), biologically independent replicates. **D** Schematic kymograph of a single-channel microfluidic device designed to trap *S. aureus* USA300 gentamicin-induced persister cells. **E** Survival plot of exponential-phase *S. aureus* USA300 lineages during primary and secondary treatments in the microfluidic mother-machine device. Persister lineages that survived the initial gentamicin exposure sustained survival during gentamicin retreatment and showed complete loss of viability over time following WP-CAMPER1-d treatment. **F** Schematic of the established murine skin infection model where treatment is initiated 24 h post-infection. **G** Bacterial burden in infected skin tissue treated with WP-CAMPER1 or WP-CAMPER1-d (2% *w*/*w*), compared with mupirocin (2% *w*/*w*) and vehicle control. For each group, data represent mean ± SD of $n = 8$, biologically independent replicates. **H** Schematic of the neutropenic deep thigh infection model. **I** Bacterial burden in thigh muscle tissue infected with stationary-phase *S. aureus* MW2 persister cells (IM), and treated intraperitoneally (IP) with vehicle control ($n = 8$, biologically independent replicates) with WP-CAMPER1-d ($n = 8$ biologically independent replicates) or WP-CAMPER1 (10 mg/Kg) ($n = 7$ biologically independent replicates), or vancomycin (30 mg/Kg) ($n = 8$ biologically independent replicates) as an antibiotic control. For data in **B**, **G**, **I**, statistical significance for comparisons between the untreated control and all treatment groups was determined using two-sided one-way ANOVA followed by Dunnett's multiple-comparisons test. Comparisons between WP-CAMPER1 and WP-CAMPER1-d were performed using an unpaired two-tailed Student's *t*-test. n.s. denotes not significant. *p* values are indicated in the graph. Source data file provided.

enzymatic degradation by host and bacterial proteases[14], we hypothesized that its D-enantiomeric variant could retain comparable antimicrobial activity, due to preservation of the key physicochemical properties prioritized by CAMPER (charge, hydrophobicity, helicity, and amphipathicity), while offering resistance to proteolytic degradation.

We synthesized WP-CAMPER1-d alongside a set of Class A peptidomimetics that preserve the overall peptide backbone structure of WP-CAMPER1 but incorporate substitutions at lysine residues with non-proteinogenic amino acids to avoid recognition and degradation by proteases. We evaluated the resulting peptide variants for activity against a panel of antibiotic-resistant *S. aureus* strains (Table 2). As

https://doi.org/10.1038/s41467-026-70348-9

Table 2 | Minimal inhibitory concentrations of WP-CAMPER1-based class A peptidomimetics against drug-resistant *S. aureus* strains

Peptide	Seq[a]	MIC (μg/mL)								HL_{50}[j]/Hemo%[k]	LD_{50}[l]/Tox%[m]
		MSSA[b]	MRSA[c]	MRSA[d]	VISA[e]	VISA[f]	VRSA[g]	C.I.[h]	C.I.[i]		
WP-CAMPER1	WKLIALLAKKLL	4	4	4	4	8	4	4	4	64[j]	128[l]
WP-CAMPER1-*d*	*WKLIALLAKKLL*	4	4	4	4	8	4	4	8	64[j]	50[l]
WP-CAMPER1-*Dab*	W*Dab*LIALLA*DabDab*LL	16	8	8	16	32	8	16	16	14[k]	99[m]
WP-CAMPER1-*Dap*	W*Dap*LIALLA*DapDap*LL	32	16	16	32	32	16	16	32	22[k]	99[m]
WP-CAMPER1-*Orn*	W*Orn*LIALLA*OrnOrn*LL	16	8	8	16	32	8	16	16	11[k]	99[m]
WP-CAMPER1-*Cyc*	WKLIALLAKKLL	>32	>32	>32	>32	>32	>32	>32	>32	2[k]	99[m]
Mel[n]	GIGAVLKVLTTGLPALISWIKRKRQQ	8	8	8	16	16	8	8	16	NA	NA

Dab diaminobutyric acid, *Dap* diaminopimelic acid, *Orn* ornithine, *Cyc* head-to-tail cyclization

[a]Peptide sequences have free N-terminus and is amidated at the C-terminus; italicized are all *d*-forms of amino acids; bold and italicized are lysine residues substituted with unnatural amino acids

[b]MSSA; *S. aureus* Newmann

[c]MRSA; *S. aureus* MW2

[d]MRSA; *S. aureus* USA300

[e]VISA; *S. aureus* ARO215

[f]VISA; *S. aureus* ARO216

[g]VRSA; *S. aureus* VRS1

[h]Clinical isolate; *S. aureus* BF1

[i]Clinical isolate; *S. aureus* BF2

[j]HL_{50}; 50% Hemolytic concentration to human RBCs

[k]Hemolysis %; percentage lysis of human RBCs at 64 μg/mL peptide concentration

[l]LD_{50}; 50% cytotoxic concentration to human HepG2 cells

[m]Toxicity %; percentage toxicity of human HepG2 cells at 128 μg/mL peptide concentration

[n]Mel; melittin

hypothesized, WP-CAMPER1-d retained antimicrobial activity comparable to that of the parent peptide WP-CAMPER1 (4–8 μg/mL), mirroring the intact physicochemical profile prioritized by CAMPER. In contrast, analogs containing diaminobutyric acid (Dab), diaminopimelic acid (Dap), and ornithine (Orn) substitutions, which disrupted the physicochemical properties prioritized by CAMPER, showed reduced potency (MIC 8–32 μg/mL), and the cyclic variant was inactive (MIC > 32 μg/mL).

Next, we tested the stability of WP-CAMPER1-d to α-chymotrypsin and its cytotoxicity against various human cell lines. WP-CAMPER1-d remained intact after 24 h of α-chymotrypsin exposure, whereas linear WP-CAMPER1 was fully degraded within 2 h (Fig. S15). Hemolysis assays showed comparable toxicity (Fig. S16). Against other human cell lines, the LD_{50} of WP-CAMPER1 was 120 μg/mL in HaCaT, 128 μg/mL in HepG2, and 55 μg/mL in HKC-8 cells. For WP-CAMPER1-d, the LD_{50} values were 65 μg/mL in HaCaT, 50 μg/mL in HepG2, and 35 μg/mL in HKC-8 cells (Fig. S17). Overall, WP-CAMPER1-d exhibited a promising anti-staphylococcal profile compared to other lysin-substituted peptidomimetics, showed proteolytic stability, and a defined therapeutic window.

We also evaluated whether *S. aureus* MW2 could develop resistance to WP-CAMPER1 and WP-CAMPER1-d. No resistance was observed after 21 serial passages, as MIC values remained unchanged (Fig. 5C). In contrast, ciprofloxacin exhibited a >4-fold MIC increase by day 15 and a >16-fold increase by day 21, indicating the emergence of resistance.

To assess the persistence of bacterial growth suppression following peptide exposure, we evaluated the post-antibiotic effect (PAE) of WP-CAMPER1 and WP-CAMPER1-d against *S. aureus* MW2. The PAE values for WP-CAMPER1, WP-CAMPER1-d, and ciprofloxacin, relative to the untreated control, were 1.68 ± 0.19 h (95% CI = 1.26–2.10) ($p = 0.0009$), 2.45 ± 0.31 h (95% CI = 1.67–3.23) ($p < 0.0001$), and 0.91 ± 0.17 h (95% CI = 0.53–1.29) ($p = 0.0047$), respectively. Notably, the PAE of WP-CAMPER1-d was significantly longer than that of WP-CAMPER1 ($p = 0.018$), confirming that D-enantiomerization prolongs post-antibiotic suppression relative to the parent peptide. These findings demonstrate that both CAMPER-derived peptides exhibit prolonged bacterial growth inhibition compared with ciprofloxacin, with WP-CAMPER1-d showing the strongest and most durable effect.

Anti-persister activity of WP-CAMPER1-d against exponential phase *S. aureus* persisters

To assess the ability of WP-CAMPER1 and WP-CAMPER1-d against persistent cells in an environment that is closer to the in vivo conditions, we used the Mother Machine, a single-cell microfluidic assay. Using this platform, we monitored ~5520 trenches, each containing ~20 exponential-phase *S. aureus* USA300 cells, and exposed them to a bactericidal concentration of gentamicin (3.75 μg/mL) (Fig. 5D, E). During the first gentamicin treatment, out of 5520 trenches analyzed across four biological replicates, only 4 trenches contained surviving lineages after treatment with a survival frequency: (4/5520, 0.072%; 95% CI: 0.019%–0.185%), exhibiting a persister-like phenotype (Fig. 5D). These results correspond to a survival frequency of 0.069% based on lineage-level analysis. However, during the second gentamicin treatment (3.75 μg/mL), the four surviving lineages from the first gentamicin treatment were exposed to a second challenge: two each for retreatment with gentamicin or with the WP-CAMPER1-d peptide (60 μg/mL) (Fig. 5D) (Supplementary Video 1). In gentamicin retreatment: both lineages survived (2/2, 100%; 95% CI: 15.811%–100%) (Supplementary Video 2 and 3), while during peptide retreatment with WP-CAMPER1-d, both lineages were eradicated (0/2, 0%; 95% CI: 0%–84.188%) (Supplementary Videos 4 and 5), indicating a differential response to the two treatment regimens (Fig. 5D, E).

In vivo efficacy of WP-CAMPER1-d in a murine biofilm and a persister infection model

Following the single-cell evidence of anti-persister activity of WP-CAMPER1-d against exponential-phase MRSA persisters, we sought to evaluate its efficacy in capturing both surface-associated and deep-tissue infections. We employed two murine infection models: a biofilm-associated skin infection and a deep-seated thigh infection model (Fig. 5F, H). In the established biofilm model, a single topical dose of WP-CAMPER1-d (2% *w/w* in white petroleum jelly), applied 24 h post-infection, significantly reduced *S. aureus* MW2 burden by 1.37 $\log_{10}$ CFU ($p < 0.0001$) (95% CI = 0.90–1.84) compared to the vehicle-treated animal group (Fig. 5G). In comparison, WP-CAMPER1 (2% *w/w*) reduced the bacterial load by 1.22 $\log_{10}$ CFU ($p < 0.0001$) (95% CI = 0.73–1.71), which was only 0.15 $\log_{10}$ CFU lower than WP-CAMPER1-d, indicating similar efficacy between L- and D- forms of WP-CAMPER1, since the difference was not statistically significant ($p = 0.496$). Meanwhile, the 2% mupirocin ointment control achieved a reduction of 2.06 $\log_{10}$ CFU ($p < 0.0001$) (95% CI = 1.54–2.58) compared to the control mice treated with white petroleum jelly (Fig. 5G). Bacterial reduction by mupirocin was 0.69 $\log_{10}$ CFU ($p = 0.0198$) (95% CI = 0.13–1.26) greater than that achieved by WP-CAMPER1-d and approximately 0.84 $\log_{10}$ CFU ($p = 0.0080$) (95% CI = 0.26–1.42) greater than WP-CAMPER1.

In the deep-seated thigh infection model, WP-CAMPER1-d (10 mg/Kg) reduced the bacterial load of stationary-phase *S. aureus* MW2 persister cells by 1.6 $\log_{10}$ CFU ($p < 0.0001$) (95% CI: 1.33–1.87), whereas WP-CAMPER1 achieved a 1.05 $\log_{10}$ reduction ($p < 0.001$) (95% CI = 0.81–1.29), compared to the vehicle treated animal group (Fig. 5I). The observed additional ~0.55 $\log_{10}$ reduction in *S. aureus* MW2 burden with WP-CAMPER1-d compared to WP-CAMPER1 ($p = 0.0029$), suggests that the enhanced enzymatic stability of the D-form may play a critical role, ultimately affecting the extent of bacterial clearance. In contrast, treatment with the control antibiotic vancomycin (30 mg/Kg) was ineffective, confirming the presence of antibiotic-tolerant persisters and validating the bacterial persistence in the deep-seated thigh infection model. We also evaluated the renal toxicity of WP-CAMPER1-d and WP-CAMPER1 by measuring serum levels of blood urea nitrogen (BUN). Neither WP-CAMPER1 nor WPCAMPER1-d led to a statistically significant increase in BUN levels compared to the vehicle-treated control group (Fig. S18).

Discussion

S. aureus is a major pathogen responsible for a broad range of hospital- and community-acquired infections[3,35–37] and commonly affects the skin, soft tissues, bones, and implanted medical devices[3,35,36]. In hospitals, *S. aureus* causes catheter-related bloodstream infections, surgical site infections, and ventilator-associated pneumonia[3,35,36]. In the community, it remains a leading cause of abscesses and invasive disease[37]. A major challenge in treating *S. aureus* infections is its ability to form biofilms and harbor persister cells that are phenotypically tolerant subpopulations that survive antibiotic treatment without resistance mutations[6–8,10]. These persisters contribute to treatment failure, chronic infection, and relapse, particularly in deep-tissue and device-associated infections[8,38,39].

Membrane-targeting AMPs have emerged as promising candidates for next-generation antibiotics[8,11], and ML is becoming a powerful tool to accelerate their discovery while reducing development costs[40,41]. In this study, we report CAMPER, a hybrid framework that combines supervised ML with a biophysically informed scoring function, to design and optimize AMPs to specifically target the bacterial cell membrane to combat persistent *S. aureus* infections. We used

CAMPER to optimize a mastoparan-derived peptide and identified WP-CAMPER1, a short peptide with strong activity against *S. aureus* MW2 and VRS1 persisters and biofilms, both in vitro and in vivo. WP-CAMPER1 acts by disrupting bacterial membranes, enabling rapid killing of dormant and biofilm-associated cells. Both the L- and D-enantiomers were effective in targeting persisters in vitro and in mouse infection models, with the D-enantiomer, WP-CAMPER1-d, demonstrating enhanced stability and superior efficacy, effectively killing exponential-phase persisters of *S. aureus* USA300 and significantly reducing *S. aureus* MW2 burden in both a topical established infection model and a deep-seated thigh infection model enriched with stationary-phase persisters.

CAMPER extends standard ML by imposing a scoring function that prioritizes candidates based on functional plausibility. The first component of CAMPER is a supervised ML classifier trained on chemically interpretable descriptors from experimentally validated AMPs, adapting an approach widely adopted in recent AMP prediction studies that leverage curated training datasets and descriptor-based feature sets[21,27,28,41–43]. Importantly, current ML-based AMP discovery methods rely on statistical associations between sequence features and activity[21,27,28,42,43], but lack mechanistic insight and, thus, do not rank predicted candidates based on the biophysical properties required for a defined mode of action (MOA), such as membrane disruption.

To focus on membrane-targeting AMPs, which are particularly promising for addressing biofilms and persister cells[44], CAMPER includes a biophysical scoring function, that evaluates four essential membrane-disruptive AMP parameters: net positive charge, helicity, amphipathicity, and hydrophobicity[14,45,46]. Each parameter plays a distinct mechanistic role, charge drives electrostatic attraction to bacterial membranes[24], helicity supports bilayer insertion[47], amphipathicity promotes interfacial alignment[48], and hydrophobicity enables deep membrane penetration[8,11]. In addition to evaluating each biophysical property individually, CAMPER captures how these properties work together by incorporating two cooperative mechanisms. First, it uses a minimum function to capture the weakest contributing property among charge, hydrophobicity, helicity, and amphipathicity, based on the principle that all are required for membrane activity and a deficiency in any one can constrain overall function[8,11,14,49]. Second, it incorporates a threshold-based boost that increases the score by a fixed amount when all four transformed scores exceed a defined cut-off, reflecting the synergistic enhancement observed when a peptide meets minimum requirements across charge, hydrophobicity, helicity, and amphipathicity. This approach ensures that peptides with consistently strong profiles across all relevant properties are rewarded, rather than relying on strength in only a subset of features.

As proof-of-concept, we applied CAMPER to a peptide library created through rational design and systematic substitutions of amino acids. However, the framework is inherently flexible and adaptable to a wide range of peptide discovery and engineering strategies. CAMPER is not limited to a single design approach and can support both de novo peptide generation and the optimization of existing scaffolds by prioritizing candidates with favorable biophysical properties linked to membrane activity. Moreover, because CAMPER operates on generalizable physicochemical principles, charge, hydrophobicity, helicity, and amphipathicity, it is agnostic to how candidate sequences are derived. This enables its application to libraries produced through evolutionary analysis[25], structure-based design[50], or sequence shuffling[51]. Furthermore, the biophysical scoring function can be tuned to reflect specific discovery objectives or microbial targets. For example, the weighting or thresholds could be modified to emphasize properties critical for outer membrane penetration in Gram-negative bacteria, or they could be adapted for selectivity against bacterial versus mammalian membranes. This target-aware adaptability makes CAMPER especially valuable for hypothesis-driven AMP development, high-throughput screening prioritization, or iterative optimization cycles.

We applied CAMPER specifically to prioritize membrane-disruptive activity, in order to address the critical clinical need for agents with activity against *S. aureus* persister cells and biofilms. To experimentally validate this design objective, we selected the top-ranked candidate, WP-CAMPER1, and conducted a series of structural and functional assays to confirm its MOA. Our CD spectroscopy of WP-CAMPER1 revealed an increase in helicity in the presence of SDS, a widely used bacterial membrane mimic[14], suggesting that WP-CAMPER1 positively associates with the model membrane. The presence of such a hydrophobic patch in WP-CAMPER1 is structurally similar to other short helical amphipathic peptides, such as DFTamP1[14] and Cry10Aa-derived peptides[52] that effectively target the bacterial membranes. The 3D solution structure of WP-CAMPER1, determined by NMR in the presence of SDS, confirmed a broad hydrophobic membrane-interacting surface.

Our biochemical assays showed that WP-CAMPER1 effectively depolarized and permeabilized live MRSA cells[53], though they did not definitively clarify the precise model adopted for membrane-targeting MOA. MD simulations with a DOPC/DOPG (7:3) model membrane indicated that WP-CAMPER1 positions itself inside the outer leaflet, parallel to the phospholipid bilayer. Unlike peptides such as melittin, which align perpendicularly and form pores[54], shorter peptides like WP-CAMPER1 that cannot span the membrane often exert their antimicrobial effects through a carpet-like mechanism[54], producing extensive membrane deformations similar to those in the SEM and cryo-TEM images[24,55].

WP-CAMPER1 physiologically impaired the ΔpH component of the PMF in *S. aureus* MW2. Disruption of the PMF in *S. aureus* has been observed in other short, helical peptides, such as LI14[56]. In addition, WP-CAMPER1 induced a significant increase in intracellular ROS content. Lethal membrane perturbation often triggers the accumulation of ROS, a stress response associated with bacterial killing[57]. Excessive ROS production can damage key cellular components, particularly through lipid peroxidation, where free radicals degrade fatty acids in the membrane, similar to the AW1, a frog-derived α-helical peptide from *Amolops wuyiensis* that has strong anti-staphylococcal activity[57]. While these effects are consistent with membrane disruption, further studies are needed to determine whether the observed oxidative stress is a direct consequence of membrane targeting or reflects additional MOA associated with WP-CAMPER1. Nevertheless, these physiological effects of WP-CAMPER1 on *S. aureus* MW2 align with our RNA-seq data, which revealed broad transcriptional changes across multiple pathways, including stress responses, energy metabolism, and a down-regulation of the oxidative phosphorylation. The full transcriptomic analysis is discussed in detail in the Supplementary Discussion.

After confirming that WP-CAMPER1 disrupts membranes and is effective in vitro and in vivo, we next evaluated its ability to eradicate persistent *S. aureus* infections in topical and systemic models. We selected membrane disruption as the MOA of interest because it offers a promising strategy to eradicate persister cells[12,30]. Persister cells are a transient subpopulation that survives high antibiotic concentrations without genetic resistance and can resume growth once the stress is removed[6,10]. In *S. aureus*, persister cells arise during planktonic growth (both in the exponential and stationary phases), as well as, within biofilms, which serve as major reservoirs of persisters that contribute to infection relapse[10,38].

To support systemic application, we synthesized WP-CAMPER1-d, the D-enantiomer of the parent peptide, together with a set of Class A peptidomimetic analogs. These peptidomimetic analogs preserved the WP-CAMPER1 backbone while substituting lysine residues with non-proteinogenic α-amino acids to enhance protease resistance[58]. This approach allowed us to address a key translational barrier: while α-helical peptides are often potent, they are also susceptible to

degradation in systemic applications[59]. The D-enantiomer preserves the charge, hydrophobicity, helicity, and amphipathicity of the peptide, while inverting chirality to render the backbone inaccessible to proteases[14,59]. WP-CAMPER1-d retained antimicrobial potency comparable to WP-CAMPER1 across drug-resistant *S. aureus* strains. It also demonstrated complete stability in the presence of α-chymotrypsin for 24 h, in contrast to the rapid degradation of the L-form. These findings confirmed that stereochemical inversion preserved function while improving pharmacological properties.

While stationary-phase and biofilm-associated persisters have been widely studied, exponentially growing cultures also harbor persister cells[31]. However, antimicrobial efficacy data for exponentially growing persisters remain limited, largely due to technical challenges in isolating and monitoring this rare subpopulation within a background of dividing cells[60]. To assess activity against exponentially growing persisters, we employed the Mother Machine, a microfluidic platform that enables high-resolution single-cell tracking of bacterial physiology[32,61]. Unlike bulk assays, this approach allows direct visualization of rare survival phenotypes in real time under tightly controlled conditions[31,32]. The continuous flow of media mimics in vivo tissue microenvironments by generating dynamic exposure patterns and antibacterial gradients[31,32]. Using this system, we showed that lineages of *S. aureus* USA300 that had survived a previous high-dose of gentamicin were susceptible to WP-CAMPER1-d. This contrasts with gentamicin retreatment, which failed to eliminate these lineages, and confirms the capacity of WP-CAMPER1-d to kill cells with a persister-like phenotype.

Our studies culminated in testing the generated peptides in a series of murine models. In a topical prophylactic model, a 2% (*w*/*w*) topical formulation of WP-CAMPER1-d significantly reduced *S. aureus* MW2 burden in an established skin-abraded murine infection model that mimics biofilm-like infections. In this model, bacterial cells form aggregated, biofilm-like structures within 24 h post-infection[24], resembling the chronic wound environment. This murine model is particularly relevant for addressing late-stage or slow-healing skin infections, such as those resulting from burn injuries[62]. Of note, burn-related injuries account for more than 4% of all emergency department visits[63], and infections remain the leading cause of mortality in burn patients, contributing to approximately 75% of burn-related deaths[64].

Finally, we confirmed the anti-persister potency of WP-CAMPER1-d using a deep-seated thigh infection model seeded with stationary-phase *S. aureus*, a validated model that more closely mimics chronic tissue infections[12]. WP-CAMPER1-d significantly reduced bacterial burden in this setting, demonstrating improved stability and tissue distribution compared to the L-form WP-CAMPER1, which was less active in deep-tissue environments. The protease resistance of the D-enantiomer likely contributed to its sustained activity, allowing it to remain effective in proteolytically active infection sites[65]. When benchmarked against other agents that have shown efficacy in this rigorous late-treatment model, WP-CAMPER1-d compares favorably. For instance, ADEP4 combined with rifampin achieves deep-tissue sterilization by activating ClpP-mediated self-digestion of persister cells[33]. However, this approach requires combination therapy and may be limited by the risk of rifampin resistance[66]. Similarly, combination treatments using gentamicin with either bithionol[12] or a retinoid analog[30], disrupt bacterial membranes and can facilitate aminoglycoside uptake, but their therapeutic use is constrained by the need for dual-drug administration, solubility challenges, and the risk of gentamicin-associated resistance. Nigericin, an ionophore, collapses the PMF and reduces persister bacterial burdens, but is toxic to mammalian cells[67]. In contrast, WP-CAMPER1-d functions as a single-agent, membrane-targeting therapy that combines potent anti-persister activity with favorable pharmacological properties. Its performance in the thigh infection model corroborates in vitro findings and provides a strong candidate among the limited set of molecules effective in chronic, protease-rich infection environments.

In summary, we developed CAMPER, a mechanistic AI framework that integrates ML with biophysical scoring to streamline the discovery of membrane-targeting AMPs. CAMPER enables the prioritization of short, potent AMP candidates by combining statistical learning with mechanistically relevant constraints on amphipathicity, helicity, charge, and hydrophobicity. We applied CAMPER to a mastoparan-derived template and designed WP-CAMPER1, which exhibited strong anti-persister and anti-biofilm activity against drug-resistant *S. aureus*. These results position WP-CAMPER1-d as a promising, systemically deliverable AMP capable of targeting persistent and biofilm-associated *S. aureus* infections that evade conventional antibiotics. Furthermore, this proof-of-concept study validates the CAMPER methodology, which integrates an ML model with biophysically informed scoring functions and offers a platform to develop stable, mechanism-driven AMPs for use in complex and refractory infections.

Methods

Approvals

All animal studies were performed in accordance with all relevant ethical regulations and were approved by the Institutional Animal Care and Use Committee (IACUC) at the Houston Methodist Research Institute (Houston, Texas, USA; protocol numbers IS00008777 and IS00008451).

Data collection and preprocessing

We collected peptide sequences with MIC measurements against *S. aureus* from the DBAASP (https://dbaasp.org/)[68] and converted all sequences to uppercase and removed duplicates to maintain consistency. We excluded sequences containing non-standard amino acid symbols. Specifically, we removed sequences that included X (any amino acid, unknown, or unspecified), B (asparagine or aspartic acid, ambiguous), Z (glutamine or glutamic acid, ambiguous), J (leucine or isoleucine, ambiguous), U (selenocysteine), and O (pyrrolysine).

In data preprocessing, we labeled peptides with MIC values of 32 μg/mL or lower as active and those with MIC values of 64 μg/mL or greater as inactive, excluding peptides with MIC values between 32 and 64 μg/mL. This binning strategy was selected to support the primary goal of CAMPER, which is to identify high-confidence peptide candidates with strong activity. MIC values between 32 and 64 μg/mL often fall into an ambiguous range that can vary by experimental conditions, and including them can introduce label noise. Broth MIC measurements commonly vary by approximately one two-fold dilution, so values that differ by a single dilution step fall within expected assay variability[69]. Because our aim was to design a selective prioritization tool to maximize precision and reduce the number of non-active peptides forwarded for synthesis and testing, we used conservative thresholds to retain only peptides with clear activity or clear inactivity. For peptides with multiple MIC measurements, we averaged their binary activity labels (0 for inactive, 1 for active) and classified peptides with a mean activity score greater than 0.5 as active, reflecting a predominance of active measurements.

Feature engineering

We evaluated three feature-engineering strategies to characterize peptide sequences: physicochemical descriptors and fingerprints. To calculate peptide descriptors, we used the RDKit[70] (version 2023.03.3) and Biopython[71] (version 1.83) libraries (Python 3.11.3). We computed a comprehensive set of physicochemical descriptors[72], including Grand Average of Hydropathy (GRAVY), helicity, hydrophobic moment, charge, topological polar surface area (TPSA), LogP, fraction of sp3 carbons, molar refractivity, hydrogen bond donors and acceptors, molecular weight, partial charges, aromatic ring count, and various Chi and Kappa indices[73]. We added each descriptor as a feature in the

dataset (Table S1). Additionally, we calculated Morgan fingerprints (2048-bit, radius 4) to represent substructure features in a binary vector format[74]. A detailed rationale for the relevance of each descriptor class to peptide biophysics and antimicrobial activity is provided in the Supplementary Methods.

Sequence *n*-grams. We generated k-mer frequency vectors from the primary amino-acid sequence to capture short-range compositional patterns. We evaluated several *n*-gram sizes and normalized counts before model training.

ProtBERT embeddings. We extracted contextual embeddings for each peptide using the ProtBERT language model[75]. We averaged token embeddings to produce a fixed-length representation of each sequence, which we used directly as input to downstream classifiers.

Model training and evaluation

We created a stratified 80–20 outer split, reserving the 20% portion as a fixed external holdout set. We used the remaining 80% of the data for model development and evaluation. We trained an RF classifier and optimized model performance using 5-fold cross-validation to select the best-performing hyperparameters. RF is an ensemble learning method that constructs multiple decision trees during training and outputs the class that is the majority vote among the trees, enhancing accuracy and reducing overfitting[76]. To compare performance with other commonly used classifiers, we trained XGBoost[77], and logistic regression with L1 Regularization (Lasso)[78] classifiers (using scikit-learn version 1.5.2) on each feature-engineering strategy described in the feature engineering section of the "Methods" section.

To prevent near-duplicate sequences from leaking across folds, we applied homology-aware 5-fold cross-validation inside the 80% training set. We computed pairwise sequence identity using the Levenshtein ratio[79], clustered peptides at the chosen identity threshold, and assigned entire clusters to the same fold. This approach ensured that homologous peptides did not appear on opposite sides of a training–validation split. To identify an appropriate sequence-identity threshold, we performed a sensitivity analysis in which we repeated the clustering and homology-aware cross-validation across multiple similarity cutoffs and compared both the resulting cluster structure and performance metrics of the RF classifier at each threshold.

We computed accuracy, precision, recall (also known as sensitivity), and F1-score to assess predictive performance. In the following formulas, TP is the number of true positives, TN is the number of true negatives, FP is the number of false positives, and FN is the number of false negatives.

Accuracy measures the proportion of correctly classified instances out of the total instances and is defined as:

$$\text{Accuracy} = \frac{\text{TP} + \text{TN}}{\text{TP} + \text{TN} + \text{FP} + \text{FN}} \tag{1}$$

Precision indicates the proportion of true positive predictions among all positive predictions, providing insight into the model's accuracy for the positive class:

$$\text{Precision} = \frac{\text{TP}}{\text{TP} + \text{FP}} \tag{2}$$

Recall (sensitivity), measures the proportion of actual positive instances that the model correctly identifies:

$$\text{Recall} = \frac{\text{TP}}{\text{TP} + \text{FN}} \tag{3}$$

The F1-score, which is the harmonic mean of precision and recall, provides a balance between the two and is especially useful when classes are imbalanced:

$$\text{F1Score} = 2 \times \frac{\text{Precision} \times \text{Recall}}{\text{Precision} + \text{Recall}} \tag{4}$$

These metrics offer a comprehensive assessment of the model's predictive performance, considering both its overall accuracy and its effectiveness in correctly classifying positive cases and making reliable positive predictions.

To assess model robustness, we performed y-randomization[80] by randomly shuffling the response variable (active/inactive) in the training dataset while keeping the feature variables unchanged. We repeated this process 100 times, evaluating model performance after each iteration. Comparing the performance of the original model to these randomized models allowed us to assess whether the observed accuracy was likely due to meaningful patterns in the data rather than random chance.

CAMPER (constraint-driven AMP engineering with ranking)

To enhance the prediction of antimicrobial activity against *S. aureus*, we developed CAMPER (**C**onstraint-driven **AMP** **E**ngineering with **R**anking), a hybrid framework that combines the RF model with a mechanistic biophysical scoring function that incorporates key physicochemical determinants of peptide-membrane interactions. This approach extended the ML model beyond statistical pattern recognition by explicitly modeling the mechanistic basis of antimicrobial activity against Gram-positive bacteria. Four critical physicochemical properties were selected based on their established roles in antimicrobial peptide (AMP) function:

Charge. Net positive charge is essential for initial electrostatic attraction to the negatively charged bacterial surface of *S. aureus*, which contains teichoic acids and negatively charged phospholipids such as phosphatidylglycerol[8]. Unlike mammalian cell membranes, which are primarily zwitterionic, the negative charge density of Gram-positive bacterial surfaces creates a selective targeting mechanism for cationic peptides. However, excessive cationic character can

potentially prevent membrane insertion by creating overly strong surface interactions and trap the peptide at the membrane surface, preventing deeper insertion and pore formation[8,11]. Thus, membrane-active peptides require a specific range of positive charge for optimal activity, with both insufficient and excessive charge reducing effectiveness[14]. We modeled this range with a Gaussian function:

$$\text{ChargeScore} = \exp\left(-\frac{\left(q - q_{\text{opt}}\right)^2}{2\sigma_q^2}\right) \tag{5}$$

Where:

- q is the peptide's net charge.
- q_{opt} is the optimal charge
- σ_q is the width parameter that determines how quickly the score decreases as charge deviates from optimal.

This function produces a maximum value of 1.0 when $q = q_{\text{opt}}$ and decreases symmetrically as charge moves away from optimal in either direction, capturing the domain knowledge that both insufficient and excessive charge reduce antimicrobial effectiveness.

Helicity. The ability to form helical structures upon membrane contact is a crucial determinant of antimicrobial activity against Gram-positive bacteria, including *S. aureus*[47]. This structural transition typically occurs at the bacterial membrane interface and enables the peptide to

organize its amino acids into an amphipathic arrangement. Structure-activity relationship studies demonstrate that peptides with helicity below a critical threshold fail to adopt the necessary conformation for membrane disruption, resulting in substantially reduced antibacterial activity[24,47]. This suggests a non-linear, threshold-dependent relationship between helicity and antimicrobial potency. We modeled this threshold effect using a sigmoid function:

$$\text{Helicity score} = \frac{1}{1+e^{-k_h\left(h-h_{\text{threshold}}\right)}} \tag{6}$$

Where:
- h is the peptide's helical propensity (0–1 scale).
- $h_{\text{threshold}}$ is the inflection point where activity begins to increase rapidly
- k_h is the steepness parameter that controls how rapidly the function transitions from low to high values.

The sigmoid function produces a smooth S-shaped curve that maps helicity to a score between 0 and 1. When helicity is well below the threshold ($h \ll h_{\text{threshold}}$), the score approaches 0. As helicity increases and crosses the threshold, the score rises rapidly, eventually approaching 1 as helicity becomes sufficiently high ($h \gg h_{\text{threshold}}$). This formulation reflects the understanding that increased helicity improves the likelihood of stable membrane interaction, supporting the peptide's ability to insert and disrupt the bilayer[81].

Hydrophobicity. Gram-positive bacterial membranes contain a higher proportion of branched-chain fatty acids compared to mammalian membranes, creating distinct hydrophobic environments[8]. Sufficient hydrophobicity, measured by the GRAVY, is essential for peptide insertion into these membrane environments. AMPs with higher

hydrophobicity values can penetrate deeper into the hydrophobic core of the bacterial membrane[82]. Similar to helicity, hydrophobicity exhibits a threshold-dependent effect, where values below a certain level prevent effective membrane insertion regardless of other properties[82]. We modeled this using another sigmoid function:

$$\text{Gravy score} = \frac{1}{1+e^{-k_g\left(G-G_{\text{threshold}}\right)}} \tag{7}$$

Where:
- G is the GRAVY value of the peptide.
- $G_{\text{threshold}}$ is the minimum effective GRAVY value.
- k_g is the steepness parameter controlling the transition rate.

This mathematical representation aligns with biophysical evidence that peptides must achieve sufficient hydrophobicity to overcome the energetic barrier of inserting into the lipid bilayer.

Amphipathicity. The spatial segregation of hydrophobic and hydrophilic residues, quantified by the hydrophobic moment (μ_H), enables peptides to simultaneously interact with both the polar headgroups and hydrophobic core of bacterial membranes[24]. For Gram-positive targets such as *S. aureus*, where peptidoglycan layers may partially shield membranes, strong amphipathicity facilitates deeper penetration and subsequent membrane disruption[8]. This property mediates multiple mechanisms of action including barrel-stave, toroidal pore, and carpet models of membrane permeabilization[8], each requiring a minimum threshold of amphipathicity to be effective. We modeled this using a sigmoid function:

$$\text{Amphipathicity score} = \frac{1}{1+e^{-k_a\left(\mu_H-\mu_{H,\text{threshold}}\right)}} \tag{8}$$

Where:
- μ_H is the hydrophobic moment, measuring the segregation of hydrophobic and hydrophilic residues.
- $\mu_{H,\text{threshold}}$ is the minimum effective hydrophobic moment.
- k_a is the steepness parameter controlling the transition rate.

Like the other sigmoid functions, this mathematical formulation produces a score that transitions from near-zero to near-one as the amphipathicity crosses the threshold value. This function models the biophysical requirement for sufficient segregation of hydrophobic and hydrophilic residues to interact effectively with bacterial membranes.

Membrane-active peptides operate through a multi-step mechanism involving initial electrostatic binding to membrane surfaces, hydrophobic insertion into the lipid bilayer, and subsequent pore formation or membrane permeabilization[82]. Each step requires simultaneous contribution from multiple physicochemical properties: charge facilitates initial membrane binding and selectivity, hydrophobicity drives insertion into the lipid core, helicity ensures proper orientation and depth, and amphipathicity interfacial alignment and peptide clustering[8,11,24,81]. This creates interdependencies where deficiency in one property cannot be compensated by excess in others, as each step requires a minimum threshold of all relevant properties to proceed effectively. We mathematically model this cooperative nature through two mechanisms:

Cooperative effect (minimum function). The minimum function captures the rate-limiting step concept in peptide-membrane interactions:

$$\text{Cooperative effect} = min\begin{pmatrix}\text{Charge score}\\ \text{Helicity score}\\ \text{Gravy score}\\ \text{Amphipathicity score}\end{pmatrix} \tag{9}$$

This function returns the lowest value among all input scores, imposing a strict constraint that the overall effectiveness cannot exceed that of the weakest component. This reflects the sequential, multi-step nature of peptide-membrane interactions, where a deficiency in any step creates a bottleneck for the entire process.

Cooperative boost (threshold function). We also implemented a threshold-based cooperative boost that captures the synergistic enhancement observed when all properties exceed minimum requirements:

$$\text{Cooperative boost} = \beta \times I(\text{all scores} > \tau) \tag{10}$$

Where:
- β is the boost magnitude.
- τ is the quality threshold.
- $I(\cdot)$ is the indicator function that equals 1 when the condition is satisfied and 0 otherwise.

This creates a step function that adds a constant bonus (β) when all component scores exceed the threshold τ and contributes nothing otherwise.

Final score calculation. The component scores were combined into a comprehensive biophysical score, which was then normalized and

integrated with the ML prediction:

$$\text{Raw biophysical score} = \sum_i w_i \times \text{Component}_i + \text{Cooperative boost} \tag{11}$$

Where w_i are the component weights for each property and cooperative term.

To ensure the biophysical score remains within the [0,1] range for consistent interpretation, we apply normalization:

$$\text{Biophysical score} = \frac{\text{Raw biophysical score}}{\sum_i w_i + \beta} \tag{12}$$

We combined the ML probability and the biophysical score using a simple weighted sum to generate the final CAMPER score:

$$\text{Final score} = w_{\text{prob}} \times \text{ML probability} + \left(1 - w_{\text{prob}}\right) \times \text{Biophysical score} \tag{13}$$

Where w_{prob} controls the balance between data-driven and mechanism-based predictions.

Optimization of the biophysical scoring function

To define meaningful threshold values for the biophysical scoring function, we utilized peptide sequences from the Antimicrobial Peptide Database (APD) (https://aps.unmc.edu/) that were active against Gram-positive bacteria and experimentally confirmed to adopt an α-helical structure[83]. For each of the four biophysical features used in the scorer (net charge, predicted helicity, hydrophobicity, and amphipathicity) we calculated the median value across this curated set. These medians were then used as the threshold parameters in the transformation functions previously defined (sigmoid for helicity, hydrophobicity, and amphipathicity; Gaussian for charge).

We then performed a grid search with five-fold cross-validation to tune the remaining hyperparameters of the scoring function. This included the steepness of the transformation functions, a threshold and weight controlling the contribution of cooperative effects between features, individual weights for each biophysical component, and a mixing weight that balances the biophysical score with the predicted probability of the RF model. Cross-validation was conducted exclusively on the training set of the RF classifier, ensuring that the test set remained untouched during parameter selection. For each hyperparameter combination, a biophysical scorer was fit to the training folds and applied to the validation fold. Performance was evaluated using ranking metrics, with precision in the top 10% of ranked peptides as the primary optimization target. The best-performing parameter set was selected based on the average cross-validated performance across all folds.

Precision analysis across biophysical property space

To evaluate how prediction precision varied across key biophysical properties, we conducted a stratified analysis of test set performance for the RF model and CAMPER. For each property, GRAVY, helicity, net charge, and hydrophobic moment, the test set was divided into eight equal-width bins spanning the observed range. Bins with fewer than 10 samples were excluded to ensure statistical robustness.

Within each bin, we calculated precision for both the RF model and the biophysically adjusted predictions. We then computed the absolute improvement in precision introduced by the biophysical adjustment. These values were used to identify regions of the property space where the biophysical integration improved prediction reliability.

Rational design of a peptide pool library

To demonstrate the ability of CAMPER to prioritize potent, membrane-active AMPs, we applied the pipeline to a candidate pool derived from a natural 14-mer template, using it as a proof of concept for targeted in silico screening. To generate the pool, we selected a mastoparan template, a 14-mer natural peptide from the wasp family, a group of amphipathic, cationic α-helical peptides found in the venom of insects of the Hymenoptera order[84]. While CAMPER can be applied to any linear peptide sequence to enhance peptide-membrane interaction through ideal amino acid substitutions, we selected this peptide template because it exhibited a distinct pattern of conserved and non-conserved amino acid positions (Fig. S19). We specifically targeted the non-conserved residues, as they were not restricted to any specific class of amino acids and could either contribute to increased net charge for electrostatic interactions or participate in hydrophobic interactions with the membrane.

While linear peptides of various lengths can be used, shorter AMP sequences are generally more cost-effective for therapeutic applications[11]. Therefore, we first optimized the sequence by removing amino acids that were unlikely to contribute to bacterial membrane binding. Specifically, to shorten the mastoparan peptide, we removed the first two N-terminal residues, isoleucine and asparagine, since they do not participate in the α-helical structure, as shown by the NMR structure of mastoparan-L in detergent micelles mimicking bacterial membranes (PDB ID: 1D7N)[85], and thus are not involved in membrane interactions critical for peptide activity (Fig. S20). This truncation yielded a 12-residue peptide template retaining three helical turns.

Next, we determined which amino acid positions in this 12-residue template could be substituted to enhance its antimicrobial potential. We aligned all known mastoparan peptide sequences to identify conserved and non-conserved amino acid positions (Fig. S19). The sequence of our 12-residue wasp derived (WP) template was (WK***X***IA***XX***AKK***X***L), where ***X*** represents the non-conserved residues (positions 3, 6, 7, and 11) (Fig. S19). We substituted these four positions with all possible amino acid combinations, generating a pool of 160,000 (20^4) peptides.

Validation of WP-CAMPER1 by traditional QSAR-based peptide design

To assess whether CAMPER successfully prioritized peptide sequences with charge, hydrophobicity, and amphipathicity profiles optimized for membrane-disruptive antimicrobial activity, we conducted a QSAR analysis of WP-CAMPER1, the top-scoring peptide from the CAMPER screen. This involved introducing targeted substitutions of hydrophilic and hydrophobic residues on distinct helical faces of the peptide to evaluate how changes in physicochemical properties affected antimicrobial potency. To assess the effect of increasing charge, we replaced leucine (non-conserved position) at position 6 on the hydrophilic face with lysine, creating WP-CAMPER1-6K. To enhance the hydrophobicity of this charged variant, we substituted alanine residues (conserved positions) at positions 5 and 8 with leucine, generating WP-CAMPER1-6K5L8L. To further increase the hydrophobicity of WP-CAMPER1-6K, we substituted tryptophan residues at positions 3, 7, and 11 (non-conserved positions) to generate WP-CAMPER1-6K3W7W11W and at positions 3, 5, 7, 8, and 11 (all hydrophobic positions) to produce WP-CAMPER1-6K3W5W7W11W. Finally, we enhanced the hydrophobicity of the hydrophobic face while keeping the overall charge of the ML-selected peptide unchanged. Starting with WP-CAMPER1 we replaced the alanine (conserved positions) at positions 5 and 8 with leucine, resulting in WP-CAMPER1-5L8L.

Bacterial strains growth conditions and peptide synthesis

We employed a panel of *S. aureus* strains exhibiting diverse antibiotic susceptibility profiles, as detailed in Table S9. All *S. aureus* strains were grown in tryptic soy broth (TSB) (BD, Franklin Lakes, NJ, USA) under

standard aerobic conditions at 37 °C with shaking unless otherwise stated.

Synthesis of peptides
We synthesized the peptides using solid-phase chemistry (GenScript Inc., Piscataway, NJ, USA). These peptides had a purity of 95% or higher (list of peptides and their characterization data can be found in Fig. S21).

Minimal inhibitory concentration (MIC) assay
We determined the MIC of candidate peptides using the broth microdilution method described by the Clinical and Laboratory Standards Institute[86]. We prepared serial dilutions of 10× concentrated peptides (10 μL) in duplicate in 96-well plates (Cat no. 3595, Corning, NY, USA). To these dilutions, we added 90 μL of logarithmic-phase bacteria at 1×10^6 CFU/mL (in TSB) and incubated the plates at 37 °C for 18 h. We then measured OD_{600} on a Spectra Max i3x spectrophotometer (Molecular Devices, CA, USA) and determined the MIC as the lowest concentration of peptides that completely inhibited bacterial growth. To assess peptide activity under various salt conditions, we incorporated physiologically relevant concentrations of salts and serum into the TSB medium, adding 150 mM NaCl, 2.5 mM $CaCl_2$, 8 μM $ZnSO_4$, 1 mM $MgSO_4$, and 5-10% human serum to medium for MIC assays.

S. aureus persister cell and time-kill assays
We generated antibiotic-induced *S. aureus* MW2 and VRS1 persister cells by following an established protocol[87]. We grew 25 ml cultures of *S. aureus* strains MW2 and VRS1 to stationary phase, then treated the cells with gentamicin at 20 μg/mL for an additional 4 h. After washing the bacterial cultures three times with 25 ml of phosphate-buffered saline (PBS), we adjusted the cultures to ~1×10^8 CFU/mL for *S. aureus* MW2 and ~1×10^7 CFU/mL for *S. aureus* VRS1 in PBS. To assess the killing kinetics of WP-CAMPER1 in persister cells, we added 1 mL of cell suspension to wells in a 2-ml deep-well assay block (Cat no. 3960, Corning, NY, USA) containing 10× MIC or 1× MIC of the peptide. We also included ciprofloxacin (at 10 μg/mL) for *S. aureus* MW2 and linezolid (100 μg/mL) for *S. aureus* VRS1 as antibiotic controls. We incubated the plates at 37 °C with shaking at 225 rpm. At specific time points (0, 15, 30, 60, and 120 min), we collected 10 μL samples, performed serial dilutions, and plated them on tryptic soy agar (TSA) (BD Difco, NJ, USA) plates. The TSA plates were incubated at 37 °C for 18 h, and then we counted resulting colonies. We conducted these experiments in duplicate. For comparison, we prepared exponential-phase cells of *S. aureus* MW2 and VRS1 in PBS and analyzed their killing kinetics in the same way as described for persister cells.

Biofilm viability assay on solid support
We generated gentamicin-induced *S. aureus* MW2 and VRS1 persister cells as outlined above. Afterward, we diluted the persister cell culture 1:200 in TSB medium supplemented with 0.2% glucose[88]. To form biofilms on substrates, we applied 1 ml of diluted bacterial culture onto a 13-mm Millipore mixed cellulose ester membrane (Cat no. HAWP01300, Millipore, MA, USA) at the bottom of a 12-well plate (Cat no. 353043, Falcon, MA, USA) and incubated it statically at 37 °C for 24 h. After incubation, we removed the planktonic cells by washing the membranes twice and transferred them to a fresh 12-well plate. We then added 1 ml of PBS containing 10× MIC concentrations of peptides and antibiotics to each well and incubated the plates under static conditions at 37 °C for another 24 h. Following this, we washed the membranes twice with PBS, placed them in 1 ml of PBS, and sonicated them in an FS 30 ultrasonic bath (Fisher Scientific, MA, USA) for 10 min. The sonicated samples were serially diluted with PBS in a 96-well plate, spot-plated onto TSA plates, and incubated overnight at 37 °C. The following day, we counted the viable bacterial colonies.

Prevention of *S. aureus* biofilm formation
We assessed the ability of the designed wasp-derived peptides to inhibit biofilm formation using an established protocol with minor modifications[87]. Briefly, we grew exponential cultures of *S. aureus* MW2 and VRS1, adjusted to $OD_{600} = 0.01$, in TSB medium supplemented with 0.2% glucose, starting from overnight cultures. We then added 90 μL of this bacterial culture to 10 μL of serially diluted 10× peptide solutions in flat-bottomed 96-well polystyrene microtiter plates (Cat no. Corning 3595, NY, USA) and incubated the plates at 37 °C for 24 h. TSB medium containing bacteria with water served as the positive control, while TSB medium with sterile water acted as the negative control. After incubation, we carefully removed the TSB medium and washed the wells with PBS (Gibco, MD, USA) to eliminate loosely attached planktonic cells. We stained the biofilms with crystal violet to quantify the biomass and determined the concentration of peptide that inhibited 50% of biofilm formation ($MBIC_{50}$). To measure the live-cell count within the biofilms, we used XTT dye [2,3-bis(2-methyloxy-4-nitro-5-sulfophenyl)−2H-tertazolium-5-carboxanilide] (ATCC, VA, USA). The percentage of biofilm growth was calculated by normalizing the biofilm growth in peptide-treated wells to that in wells containing untreated bacteria[89].

Disruption of *S. aureus* established biofilms
We evaluated the ability of the designed peptides to disrupt established biofilms following an established protocol with modifications[87]. We prepared exponential cultures of *S. aureus* MW2 and VRS1 and adjusted to 1×10^6 CFU/mLin TSB medium supplemented with 0.2% glucose from overnight cultures. We then added 100 μL of this bacterial culture to flat-bottomed 96-well polystyrene microtiter plates (Cat no. 3595, Corning, NY, USA) and incubated the plates statically at 37 °C for 24 h to allow biofilm formation. After incubation, we carefully removed the TSB medium and gently washed the wells with PBS (Gibco, MD, USA) to eliminate loosely attached planktonic cells. We treated the established biofilms with 10 μL of serially diluted 10× peptide solutions and added 90 μL of TSB medium supplemented with 0.2% glucose to each well. The plates were incubated for an additional 24 h at 37 °C before processing the biomass and live-cell content. We then calculated the concentration of peptide required to disrupt 50% of the established biofilms ($MBEC_{50}$).

Fluorescence microscopy of WP-CAMPER1-treated *S. aureus* established biofilms
We performed fluorescence microscopy on WP-CAMPER1-treated *S. aureus* biofilms using a previously described protocol with modifications[24]. In brief, we prepared exponential-phase cultures of *S. aureus* MW2 and VRS1, adjusting the bacterial count to 1×10^6 CFU/mL in fresh TSB medium. To establish biofilms, we added 200 μL of the bacterial culture to the chambers of Millicell EZ Slides (Millipore Sigma, MA, USA) and incubated them statically at 37 °C for 24 h. After incubation, we carefully removed the TSB medium and gently washed the Millicell wells with PBS (Gibco, MD, USA) to eliminate loosely attached planktonic cells. We then treated the established biofilms with 20 μL of WP-CAMPER1 peptide (at 10× MIC) and added 180 μL of TSB medium. The Millicell slides were incubated for an additional 24 h at 37 °C. Following this, we gently washed the Millicell slides with PBS to remove planktonic cells and stained the biofilms with 50 μL of staining reagent from a LIVE/DEAD kit (Life Technologies, OR, USA) according to the manufacturer's instructions. We visualized the biofilms using a Nikon ECLIPSE Ti fluorescent microscope (Melville, NY, USA) and processed the images with NIS-Elements AR 4.00.07 software (Nikon, Tokyo, Japan).

Mammalian cell cytotoxicity assays
We assessed the ability of the peptides to induce hemoglobin leakage in human red blood cells using a previously established method[90].

First, we washed human erythrocytes (Rockland Immunochemicals, PA, USA) three times with an equal volume of PBS and resuspended them in a 4% solution. We then added 100 μL of this cell suspension to 100 μL of a 2× peptide solution in a 96-well microtiter plate (Cat no. 3595, Corning, NY, USA) and incubated the plates at 37 °C for 1 h. Following incubation, we centrifuged the plates at 500× g for 5 min, transferred 100 μL of the supernatant to a new 96-well plate, and measured the absorbance at 540 nm. We calculated the percent hemolysis using the formula: (A_{540} nm of peptide solution − A_{540} nm of PBS) / (A_{540} nm of 1% Triton X-100 − A_{540} nm of PBS) × 100, where 100% hemolysis was defined by 1% Triton X-100 and 0% hemolysis was defined by PBS.

We used liver-derived HepG2 cells (Cat. No. HB-8065, American Type Culture Collection, Manassas, VA, USA), human keratinocytes (HaCaT) (Cat. No. T0020001, Fisher Scientific, MA, USA), and human kidney cortical (HKC-8) cells (courtesy of Dr. Racusen of John Hopkins University, Baltimore, MD) to evaluate the cytotoxicity of AMP based on an established protocol[90]. We cultured HepG2, HaCaT, and HKC-8 cells at 37 °C with 5% CO_2 in Dulbecco's Modified Eagle Medium (DMEM) supplemented with 10% heat-inactivated fetal bovine serum and 1% penicillin/streptomycin (Gibco, MA, USA). At ~85% confluence, cells were harvested, resuspended in fresh DMEM medium and seeded at 1×10^6 cells/well in a 96-well plate (Cat no. 3598, Corning, NY, USA) for 24 h at 37 °C with 5% CO_2. Cells were subsequently treated with 100 μL two-fold serially diluted peptides in DMEM for an additional 24 h. After treatment, 70 μL of the XTT-electron coupling reagent mixture (CyQUANT™ XTT cell viability assay kit (Fisher Scientific, MA, USA) was added to each well and incubated for 4 h. Absorbance was measured at 450 nm and 660 nm using the SpectraMax 250 plate reader (Molecular Devices, San Jose, CA, USA).

CD

We recorded the CD spectra of WP-CAMPER1 (0.2 mg/mL) in the presence and absence of 50 mM SDS using a Jasco J-815 CD Spectropolarimeter (Jasco, OK, USA) according to a previously described method in ref. 91. We placed the samples in a thermostat cell holder set to 25 °C, using a quartz cell with a 1-mm path length. The CD data were expressed as mean residue ellipticity. We obtained baseline scans under the same conditions for samples containing only buffer, micelles, and vesicles, and subtracted these baseline scans from the data obtained with peptide-containing samples.

Nuclear magnetic resonance (NMR)

We investigated the membrane-targeting mechanism of WP-CAMPER1 using two-dimensional nuclear magnetic resonance (2D-NMR) spectroscopy, following a previously published method with minor modifications[59]. We collected the NMR data at 25 °C on a Bruker Avance II 500 MHz NMR spectrometer (Bruker, MA, USA), using 600 μL of 2 mM WP-CAMPER1 dissolved in 80 mM deuterated SDS (SDS-d25; pH 5.5). We selected SDS micelles to mimic an anionic, membrane-like environment and to stabilize the peptide for structural analysis as SDS provides high spectral resolution for backbone assignments and has been widely used in NMR studies to determine the structures of AMPs[14,92,93]. We acquired homonuclear 2D-total correlation spectroscopy (TOCSY) with an 80 ms mixing time and nuclear Overhauser effect spectroscopy (NOESY) with a 300 ms mixing time, 5000 Hz spectral widths in both dimensions, and 512 increments in the indirect dimension. We also collected natural abundance 2D-^{13}C-heteronuclear single quantum coherence (HSQC) and ^{13}C-HSQC-TOCSY spectra with 128 scans to obtain ^{13}C chemical shifts, which we used to derive the dihedral angles of the peptide using TALOS + [94]. We processed and analyzed all NMR data using Topspin software version 3.2 (Bruker, MA, USA) and Sparky software version 3.115 (UCSF, CA, USA). A semi-automated assignment of NOESY cross-peaks was conducted using CYANA version 3.98.15[95], and all assigned peaks were manually verified for accuracy in Sparky. We performed the initial peptide structure calculation with 254 NOE-derived distance restraints and 22 dihedral angles. In the final calculation, we included 14 hydrogen bond restraints supported by NOESY patterns. We used 200 structures for the final calculation and selected the 20 lowest-energy structures to represent the WP-CAMPER1 structure ensemble.

MD simulation

We conducted MD simulations using membrane bilayers composed of DOPC (1,2-dioleoyl-sn-glycero-3-phosphocholine) and DOPG (dioleoyl phosphatidylglycerol) at a 7:3 molar ratio, with each bilayer containing 64 lipids[12]. We generated the initial WP-CAMPER1 structure using the AlphaFold2 Colab server[96] and positioned the peptide parallel to the membrane surface, at least 1.5 nm above the upper leaflet. The simulations proceeded in two stages[97]. First, we performed coarse-grained (CG) MD simulations using the MARTINI 2.2 P force field for 500 ns to capture membrane-peptide association[98]. We then selected representative CG frames corresponding to key events, specifically the initial membrane contact and the fully engaged state at 500 ns, and converted them into all-atom models. These all-atom systems were subsequently simulated for 10 ns using the CHARMM36 force field[98]. All simulations were carried out using the GROMACS 2020.1-1 software package (Groningen, Netherlands), with system input files generated through the CHARMM-GUI server. We visualized the trajectories using visual molecular dynamics (VMD)[99] and the trial version of BIOVIA Discovery Studio Visualizer (Accelrys Inc., SD, USA). We also simulated WP-CAMPER1 in membrane composed of POPG (1-palmitoyl-2-oleoyl-sn-glycero-3-phospho-(1'-rac-glycerol) and CL (cardiolipin) (7:3 molar ratio), following the same protocol used for the DOPC:DOPG system, to evaluate its interactions with a bilayer enriched in PG and CL, the major anionic phospholipids of *S. aureus* membranes[100].

Membrane depolarization

We measured bacterial membrane potential following an established protocol with minor modifications[90]. We prepared an exponential phase culture of *S. aureus* MW2 in fresh TSB medium, washed the culture twice with PBS, and then resuspended it in twice the volume of PBS. To energize the bacterial cells, we added 25 mM glucose and incubated them for 15 min at 37 °C. Next, we introduced 500 nM of DiBAC4(3) (bis-(1,3-dibutylbarbituric acid) trimethine oxonol) (Thermo Fisher Scientific, ON, Canada), a potential-sensitive probe that enters depolarized cells, binds to intracellular proteins or membranes, and exhibits enhanced fluorescence. We distributed 90 μL of the prepared bacterial culture into each well of a black, clear-bottomed 96-well plate (Cat. no. 3904, Corning, NY, USA) and monitored the fluorescence using a SpectraMax i3x (Molecular Devices, CA, USA) for 20 min, with excitation at 485 nm and emission at 520 nm, until a stable baseline was established. Afterward, we added 10 μL of serially diluted peptide solutions and recorded the fluorescence for an additional 40 min. We used Triton X-100 (1%) as a positive control.

SYTOX-based cell membrane permeability assay

We prepared exponential-phase *S. aureus* MW2 cells and diluted them in PBS to an OD_{600} of 0.2. We then added SYTOX Green (Molecular Probes, Life Technologies, Oregon, USA) to the cell suspension, achieving a final concentration of 5 μM, and incubated the mixture for 30 min at room temperature in the dark, following a previously established protocol[89]. We distributed 90 μL of this dye/bacteria mixture into 10 μL of serially diluted 10× peptide solutions in black 96-well plates and measured the fluorescence for 1 h at room temperature, using excitation and emission wavelengths of 485 nm and 525 nm, respectively.

Propidium iodide-based membrane permeability

We utilized a propidium iodide (PI) fluorescence-based bacterial permeation assay to investigate membrane-targeting interactions with the

designed peptides, following a previously established protocol[89]. We prepared exponential-phase *S. aureus* MW2 bacteria as described for the SYTOX assay, except that the final bacterial density was $OD_{600} = 0.4$ in PBS. We added PI dye to the bacterial suspension to achieve a final concentration of 2 μM. We measured fluorescence using excitation at 584 nm and emission at 620 nm for 1 h at room temperature.

ATP release assay
To assess the ATP leakage potential of the peptides, we used a luciferase-based assay[101]. We began by washing exponential-phase *S. aureus* MW2 bacteria three times with PBS (pH 7.4) and then adjusted the cell suspension to an OD600 of 0.4 in PBS. After treating the bacteria with 32 μg/mL of WP-CAMPER1 peptide at 37 °C for 30 min, we centrifuged the cells at 14,000×*g* for 5 min. We transferred 50 μL of each supernatant to black, clear-bottomed 96-well plates containing 50 μL of BacTiter-Glo reagent (Promega, WI, USA) and measured the luminescence after 5 min of incubation at room temperature, as previously described in ref. 101.

ΔpH measurement
We cultured *S. aureus* MW2 bacteria to mid-logarithmic phase, centrifuged the exponential-phase bacterial suspensions, and washed the cells three times with PBS (Gibco, MA, USA). We then resuspended the cells to an OD_{600} of 0.4 and incubated them with BCECF (1 μM) in the dark for 30 min at 37 °C. After staining, we treated the cells with peptides for 1 h at 37 °C. We measured fluorescence intensity at 525 nm (excitation at 485 nm) using a Cytation 3 imaging reader (BioTek Instruments, VT, USA).

ROS detection assay
We quantified ROS levels in peptide-treated *S. aureus* MW2 using the fluorescent probe 2′,7′-dichlorofluorescein diacetate (DCFH-DA), a commonly used indicator of intracellular ROS[57]. We cultured *S. aureus* MW2 to mid-logarithmic phase, washed the cells three times, and resuspended them in PBS (Gibco, MA, USA) to an OD_{600} of 0.4. We then stained the cells with DCFH-DA (100 μM) and co-incubated them with peptides at 10× MIC for 30 min at 37 °C. We measured fluorescence intensity at 525 nm (excitation at 485 nm) using a Cytation 3 imaging reader (BioTek Instruments, VT, USA).

ROS-associated growth inhibition and spot titer assays
We evaluated the role of ROS in the antibacterial activity of peptides using spot titer and kinetic growth curve assays, following a previously established protocol[57] with minor modifications. In a microplate growth curve assay, exponential-phase cultures of *S. aureus* MW2 were adjusted to 1×10^6 CFU/mL and incubated in 96-well plates (100 μL per well) with WP-CAMPER1 (1× MIC) in the presence or absence of NAC (10 mM). The optical density at 600 nm was recorded every 2 h to monitor bacterial growth kinetics using the SpectraMax 250 plate reader (Molecular Devices, San Jose, CA, USA). A decrease in bacterial killing efficiency in the presence of ROS scavengers indicated that ROS played a contributory role in the antibacterial mechanism of WP-CAMPER1[57].

In a complementary spot titer assay, exponential-phase *S. aureus* MW2 cultures were grown in TSB and diluted to approximately 1×10^6 CFU/mL. The bacterial suspensions were exposed to WP-CAMPER1 at 1× MIC in the presence or absence of the ROS scavenger NAC (10 mM). Cultures were incubated at 37 °C, and samples were collected at 0, 4, and 8 h, serially diluted, and plated on Ramel™ TSA plates (Fisher Scientific, MA, USA) to determine surviving CFU after overnight incubation.

To assess the effect of higher bacterial and peptide concentrations, we also exposed 1×10^7 CFU/mL cultures to WP-CAMPER1 at 5× MIC, with or without NAC (10 mM). Samples were collected at 0, 4, and 18 h, and 20 μL from the culture was serially diluted, and plated on Ramel™ TSA plates (Fisher Scientific, MA, USA) to quantify bacterial survival.

Lipid peroxidation assay
We assessed lipid peroxidation in *S. aureus* MW2 following peptide treatment using the fluorescent probe C11-BODIPY. We cultured the bacteria to mid-logarithmic phase, washed the cells three times, and resuspended them in PBS (Gibco, MA, USA) to an OD_{600} of 0.4. The cells were then stained with C11-BODIPY (2 μM) and co-incubated with peptides at 10× MIC for 30 min at 37 °C. Fluorescence intensity was recorded at 525 nm (excitation at 485 nm) using a Cytation 3 imaging reader (BioTek Instruments, VT, USA).

Scanning electron microscopy (SEM)
We employed a modified established protocol to perform SEM imaging of *S. aureus* MW2 bacteria treated with the WP-CAMPER1 peptide[102]. We treated 2 mL of an exponential-phase *S. aureus* MW2 culture ($OD_{600} = 0.4$, washed and resuspended in PBS) with 10× MIC of WP-CAMPER1 for 1 h at 37 °C. Following treatment, we centrifuged the bacterial cultures at 13,000× g for 10 min at room temperature. We fixed the bacteria with 50 μL of a fixing solution containing 2.5% glutaraldehyde in PBS buffer (pH 7.3) for over 1 h at room temperature. After fixation, we placed a 20 μL droplet of the sample onto a (3-Aminopropyl) triethoxysilane (APTES)-functionalized silicon wafer and incubated it for 1 h. We then thoroughly washed the silicon substrate in PBS (pH 7.3). To dehydrate the samples, we sequentially exposed the substrate to ethanol solutions of 20%, 40%, 60%, 90%, and 100% (*v*/*v* in water) for 5 min each. We then immersed the samples in tert-butyl alcohol (50% *v*/*v* in ethanol) for 5 min and allowed them to air dry. We mounted the samples on an aluminum SEM sample holder using double-sided carbon conductive tape. To improve the contrast of the SEM images, we coated the samples with a 5 nm thick Pt/Pd film using a magnetron 208HR High Resolution sputtering coater. We visualized the samples using a Nava Nano SEM 230 with a working distance of 5 mm, operating at room temperature and high vacuum (2E-6 Torr). During imaging, we set the electron beam diameter to 3 nm and the acceleration high voltage to 5 kV.

Cryo-electron microscopy (cryo-EM)
We treated a 10 mL exponential-phase *S. aureus* MW2 culture ($OD_{600} = 0.4$, washed and resuspended in PBS) with WP-CAMPER1 at 20× MIC for 1 h at 37 °C. For cryo-EM, bacterial samples were vitrified using a Leica EM-GP2® plunger (Leica Microsystems, Wetzlar, Germany) on R2 × 2 Quantifoil® carbon holey film grids (Micro Tools GmbH, Jena, Germany), following established protocols[103]. In brief, 4 μL of the treated suspension was applied to plasma-cleaned grids (Gatan Solarus 950), blotted with filter paper, and plunge-frozen in liquid ethane. Grids were stored in liquid nitrogen until imaging. For microscopy, grids were loaded into a JEM 2200FS electron microscope (JEOL Ltd, Akishima, Japan) operating at 200 keV, equipped with a field emission gun, an omega-type in-column energy filter, and a DE20 direct electron detector (Direct Electron Inc., CA, USA). Images were acquired using a 20 eV energy slit width, with a total electron dose of ~15 $e^-/Å^2$ and a pixel size of 3.66 Å at the specimen level.

Use of *S. aureus* transposon mutants
We utilized *S. aureus* transposon mutants obtained from the NTML[104]. This library includes 1952 strains, each carrying a single mutation in a nonessential gene of the USA300 strain, a community-associated MRSA isolate[104]. We specifically chose a mutant with a transposon insertion in the *fmtc* gene, which is responsible for transferring a lysyl group from L-lysyl-tRNA to membrane-bound phosphatidylglycerol (PG) to form lysylphosphatidylglycerol (LPG)[59]. LPG reduces the negative charge on the membrane, thereby enhancing bacterial

virulence by providing a resistance mechanism against cationic AMPs[59].

RNAseq assays

For RNA sequencing studies, we adhered to the protocol recommended by Novogene (Sacramento, CA, USA)[105]. We started with exponential cultures of *S. aureus* MW2 grown in TSB medium and adjusted to OD_{600} = 0.4. We treated 10 mL of this bacterial culture with 0.5× MIC of WP-CAMPER1 or water as a negative control for 30 min at 37 °C with shaking at 180 rpm. Following treatment, we washed the bacteria three times with PBS and stored the pellet at −80 °C. We extracted total RNA from the pellet and assessed its purity using a NanoPhotometer® spectrophotometer. RNA integrity and concentration were evaluated with the RNA Nano 6000 Assay Kit using a Bioanalyzer 2100 system. We also checked RNA degradation and contamination on 1% agarose gels. For transcriptome sequencing, we prepared libraries using 1 μg of RNA per sample with the NEBNext® UltraTM RNA Library Prep Kit for Illumina® (NEB, MA, USA). We started by purifying mRNA from total RNA with poly-T oligo-attached magnetic beads and then fragmented it using divalent cations in NEBNext First Strand Synthesis Reaction Buffer (5×). We synthesized cDNA using random hexamer primers and M-MuLV Reverse Transcriptase for the first strand, followed by DNA Polymerase I and RNase H for the second strand[106]. Overhangs were converted to blunt ends with exonuclease/polymerase activities. We then adenylated the 3′ ends of the DNA fragments and ligated NEBNext Adapters with hairpin loop structures for hybridization. To select cDNA fragments of the preferred length (150-200 bp), we purified the library fragments using the AMPure XP system (Beckman Coulter, CA, USA). Next, to the size-selected, adapter ligated cDNA, we added 3 μL USER Enzyme (NEB, MA, USA) at 37 °C for 15 min followed by 5 min at 95 °C before carrying out the polymerase chain reaction (PCR). We performed the PCR with Phusion High-Fidelity DNA polymerase, Universal PCR primers, and Index (X) Primer. We purified the PCR products with the AMPure XP system (Beckman Coulter, CA, USA) and assessed library quality using the Agilent Bioanalyzer 2100 system (Agilent Technologies, CA, USA).

Fabrication and surface treatment of microfluidic devices for exponential phase MRSA persister killing

A silicon wafer master mold and a polydimethylsiloxane (PDMS)-based microfluidic device were manufactured as previously described in ref. 61. To inhibit biofilm formation during imaging, the lanes of the microfluidic device were pretreated with 0.1 M EDTA (Sigma Aldrich, MO, USA) for 10 min, Biofloat Flex coating solution (facellitate) for 30 min, and rinsed with MOPS buffer[61]. For bacterial culture and cell loading, *S. aureus* USA 300 strain was grown overnight in TSB supplemented with 800 μg/mL Pluronic® F108 (Sigma-Aldrich, MO, USA) at 37 °C and 220 rpm using an Excella E24 incubator shaker (New Brunswick Scientific, NJ, USA). Cells were loaded into the microfluidic device using gel-loading tips (Fisherbrand™, NH, USA) by pipetting small volumes of culture directly into two lanes. To promote uniform cell loading into the device trenches, the chip was mounted onto a custom 3D-printed holder and centrifuged at 500 g for 5 min followed by 500 g for 15 s in the opposite direction, as previously described in ref. 61. After loading, and prior to imaging, excess inoculum was flushed out with fresh TSB containing 800 μg/mL Pluronic® F108.

For media delivery and antibiotic treatment, each lane was connected to a media reservoir flask with 0.02-inch internal diameter and 0.06-inch outer diameter Tygon tubbing (ND 100-80 Microbore Tubing, US plastic, OH, USA) and gauge 20, 1-inch, 90° stainless steel blunt Luer-lock needles (McMaster, GA, USA). A flow rate of 20 μL/min was maintained using an independent peristaltic pump in each lane (Longer Pump, Hebei Province, China).

The experiment followed a staged media exchange protocol. During the first 4 h, all device lanes were perfused with TSB containing 800 μg/mL Pluronic® F108. Subsequently, the media was switched for 4 h to TSB with the same Pluronic® F108 concentration supplemented with 3.75 μg/mL of gentamicin, which represented fifteen times the MIC for *S. aureus* USA 300 in a broth microdilution assay. Following exposure, the cells were incubated for an additional 16 h in fresh TSB with 800 μg/mL Pluronic® F108 to assess gentamicin survival. Lanes with surviving trenches were further treated for 4 h with either TSB with 800 μg/mL Pluronic® F108 and 60 μg/mL WP-CAMPER1-d, which also corresponds to fifteen times the bulk MIC, or TSB with 800 μg/mL Pluronic® F108 and 3.75 μg/mL gentamicin. This second treatment was followed by a final wash in TSB with 800 μg/mL Pluronic® F108 to evaluate bacterial survival.

For microscopy, image acquisition, and image analysis, phase contrast live-cell imaging was performed using the same microscope as described in ref. 61. Images were analyzed using a custom Python-based pipeline called TrenchCoat, as previously described in ref. 61. All image processing and data extraction were performed on the O2 high-performance computing (HPC) cluster at Harvard Medical School, MA, USA, which enabled parallel processing of large datasets. The resulting trench detection tables were used to generate kymographs using an additional custom-built Python script and FIJI macro.

For survival quantification and trench counts, the initial number of trenches was estimated by multiplying the number of FOVs imaged by 60 trenches per FOV. This method includes all trenches present in each FOV, regardless of whether a particular trench was empty at the beginning of imaging. Lineage survival was assessed visually after each first and second antibiotic treatment, based on the presence or absence of dividing cells in each trench. During non-antibiotic periods, we assumed that no cell death happened.

Serial passage assay

We evaluated the potential of WP-CAMPER1 and WP-CAMPER1-d to induce resistance in *S. aureus* MW2 using a serial passage assay adapted from a published protocol[107]. On Day 1, we performed a standard MIC assay to establish baseline susceptibility. We defined bacterial growth as an OD600 ≥ 0.35. On each subsequent day, we initiated new cultures from the well that showed visible growth (OD600 ≥ 0.35) at the highest drug concentration. We diluted the selected culture 1:1000 in fresh TSB medium and performed a new MIC assay with a concentration gradient of the peptide or the control antibiotic. We repeated this procedure for 21 consecutive days. We included ciprofloxacin as a reference antibiotic. We recorded MIC values daily to track any changes in susceptibility over time.

PAE

We evaluated the PAE of WP-CAMPER1, WP-CAMPER1-d, and ciprofloxacin against *S. aureus* MW2 following previously published methods[108,109] with minor modifications. Briefly, overnight cultures of *S. aureus* MW2 were grown in TSB at 37 °C with shaking (220 rpm) and diluted in fresh TSB to obtain an inoculum of 2×10^8 CFU/mL. We treated each 1 mL culture with WP-CAMPER1, WP-CAMPER1-d, or ciprofloxacin at 5× MIC for 1 h at 37 °C with shaking at 220 rpm. After treatment, we centrifuged the cultures at 16,000× g for 5 min to remove residual drug and washed the pellets three times with fresh TSB. The washed cultures were resuspended in drug-free TSB and incubated at 37 °C with shaking (220 rpm) to allow regrowth. We collected samples immediately before and after drug removal and then at 1 h intervals. At each time point, we removed 10 μL of culture, performed serial dilutions in PBS, and plated them on TSA plates (BD Difco, NJ, USA). Plates were incubated overnight at 37 °C, and CFU were enumerated the following day. We calculated the PAE using the

formula: PAE = *T-C*, where T was the time required for the treated culture to increase by 1 $\log_{10}$ CFU/mL from the count immediately after drug removal, and C was the corresponding time for the untreated control. Each assay, including its control, was performed in triplicate.

In vivo murine skin infection and treatment

We adapted a topical skin-abraded murine infection model with minor modifications to assess the in vivo efficacy of the WP-CAMPER1-designed peptides[110]. Female C57BL/6 mice (6 weeks old; Jackson Laboratory, Bar Harbor, ME, USA) were anesthetized via intraperitoneal injection of ketamine (90 mg/Kg) and xylazine (10 mg/Kg). The dorsal skin (~ 2 cm^2) was shaved and tape-stripped seven times using Tensoplast® tape (replacing the tape each time) to disrupt the skin barrier and create a visibly damaged surface. To initiate infection, we applied 1×10^7 CFU of *S. aureus* MW2 (exponential phase, suspended in PBS) in a 50 μL inoculum directly onto the damaged skin. For treatment, we applied 30 mg of peptide ointment (1% or 2% *w/w* in white petroleum jelly; Fisher Scientific, Cat. No. 19-090-843) at either 10 min post-inoculation (prophylactic model) or 24 h post-inoculation (established infection model). Control groups received either petroleum jelly alone (negative control) or 2% commercial mupirocin ointment (positive control). Buprenorphine SR (0.5 mg/Kg) was administered for analgesia.

After 24 h of treatment, mice were euthanized, and approximately 2 cm^2 of infected skin was excised. The skin tissue was homogenized in 1 mL PBS (Gibco), and 100 μL of the homogenate was serially diluted, plated on Ramel™ TSA plates (Fisher), and incubated at 37 °C for 18 h to quantify viable bacteria. For cytokine analysis, 10 μL of EDTA-free protease inhibitor cocktail (Set III, Millipore Sigma) was added to 500 μL of the homogenate. Cytokine concentrations were quantified by Cytokine Core, LLC (Indianapolis, IN, USA) using a Luminex® MagPix™ platform following their in-house protocol[111].

Deep-seated mouse thigh infection model

We evaluated the in vivo efficacy of WP-CAMPER1-designed peptides against *S. aureus* MW2 persisters using a modified neutropenic mouse thigh infection model[12]. We rendered six-week-old female CD-1 mice (~25 g, Charles River Laboratories, Wilmington, MA, USA) neutropenic by administering cyclophosphamide intraperitoneally at 150 mg/kg on day−4 and 100 mg/kg on day−1 before infection. On the day of infection, we washed overnight cultures of *S. aureus* MW2 three times with sterile saline and diluted them to ~10^7 CFU/mL. We injected 50 μL of the bacterial suspension into the right thigh muscle of each mouse. At 24 h post-infection, we treated mice intraperitoneally every 12 h for 3 days with either sterile water (vehicle control), WP-CAMPER1 or WP-CAMPER1-d (10 mg/Kg), or vancomycin (30 mg/Kg). We euthanized the animals at 96 h post-infection. We collected blood via cardiac puncture to assess renal toxicity and excised the infected thighs aseptically. We weighed and homogenized the thigh tissue in PBS. For bacterial quantification, we serially diluted the samples, plated them on Remel™ TSA plates (Fisher Scientific, MA, USA), and incubated them at 37 °C for 18 h. We expressed bacterial load as CFU per gram of thigh tissue. We analyzed BUN (Life Technologies, MD, USA) levels using commercial kits according to the manufacturers' protocols to evaluate liver and kidney function.

Statistical analysis

We used two-sided one-way ANOVA to compare multiple experimental groups or a two-tailed unpaired Student's *t*-test to compare values between two groups. We considered a *P* value of less than 0.05 as statistically significant for all experiments.

Reporting summary

Further information on research design is available in the Nature Portfolio Reporting Summary linked to this article.

Data availability

The RNA-seq data generated in this study have been deposited in the National Center for Biotechnology Information (NCBI) Sequence Read Archive (SRA) under accession code PRJNA1282775. The RNA-seq data are freely available without restriction. Values for all data points presented in the figures are provided in the Source Data file. The processed data generated in this study are included in the Source Data file and Supplementary Information associated with this article. Source data are provided with this paper.

Code availability

The code generated in this study has been deposited in Zenodo and is available at: https://doi.org/10.5281/zenodo.17781367.

References

1. Centers for Disease Control and Prevention. *Antimicrobial Resistance* https://www.cdc.gov/antimicrobial-resistance/index.html (2019).
2. National Academies. *Examining the Long-Term Health and Economic Effects of Antimicrobial Resistance in the United States* https://www.nationalacademies.org/our-work/examining-the-long-term-health-and-economic-effects-of-antimicrobial-resistance-in-the-united-states (2022).
3. Tong, S. Y. C., Fowler, V. G., Jr., Skalla, L. & Holland, T. L. Management of *Staphylococcus aureus* bacteremia: a review. *JAMA* https://doi.org/10.1001/jama.2025.4288 (2025).
4. Centers for Disease Control and Prevention. *Infection Control Guidance: Preventing Methicillin-Resistant Staphylococcus aureus (MRSA) in Healthcare Facilities* https://www.cdc.gov/mrsa/hcp/infection-control/index.html (2025).
5. From the Centers for Disease Control and Prevention. Vancomycin resistant *Staphylococcus aureus*—Pennsylvania, 2002. *JAMA* **288**, 2116 (2002).
6. Conlon, B. P. et al. Persister formation in *Staphylococcus aureus* is associated with ATP depletion. *Nat. Microbiol.* **1**, 16051 (2016).
7. Otto, M. Staphylococcal biofilms. *Microbiol. Spectr.* **6**, https://doi.org/10.1128/microbiolspec.GPP3-0023-2018 (2018).
8. Ganesan, N., Mishra, B., Felix, L. & Mylonakis, E. Antimicrobial peptides and small molecules targeting the cell membrane of *Staphylococcus aureus*. *Microbiol. Mol. Biol. Rev.* **87**, e0003722 (2023).
9. Xuan, J. et al. Antimicrobial peptides for combating drug-resistant bacterial infections. *Drug Resist. Updat.* **68**, 100954 (2023).
10. Lewis, K. Persister cells. *Annu Rev. Microbiol.* **64**, 357–372 (2010).
11. Mishra, B., Reiling, S., Zarena, D. & Wang, G. Host defense antimicrobial peptides as antibiotics: design and application strategies. *Curr. Opin. Chem. Biol.* **38**, 87–96 (2017).
12. Kim, W. et al. A selective membrane-targeting repurposed antibiotic with activity against persistent methicillin-resistant *Staphylococcus aureus*. *Proc. Natl. Acad. Sci. USA* **116**, 16529–16534 (2019).
13. Panahi Chegini, P., Nikokar, I., Tabarzad, M., Faezi, S. & Mahboubi, A. Effect of amino acid substitutions on biological activity of antimicrobial peptide: design, recombinant production, and biological activity. *Iran. J. Pharm. Res.* **18**, 157–168 (2019).
14. Mishra, B. & Wang, G. Ab initio design of potent anti-MRSA peptides based on database filtering technology. *J. Am. Chem. Soc.* **134**, 12426–12429 (2012).
15. Vora, L. K. et al. Artificial intelligence in pharmaceutical technology and drug delivery design. *Pharmaceutics* **15**, 1916 (2023).
16. Dara, S., Dhamercherla, S., Jadav, S. S., Babu, C. M. & Ahsan, M. J. Machine learning in drug discovery: a review. *Artif. Intell. Rev.* **55**, 1947–1999 (2022).
17. Bhadra, P., Yan, J., Li, J., Fong, S. & Siu, S. W. I. AmPEP: sequence-based prediction of antimicrobial peptides using distribution

patterns of amino acid properties and random forest. *Sci. Rep.* **8**, 1697 (2018).
18. Meher, P. K., Sahu, T. K., Saini, V. & Rao, A. R. Predicting antimicrobial peptides with improved accuracy by incorporating the compositional, physico-chemical and structural features into Chou's general PseAAC. *Sci. Rep.* **7**, 42362 (2017).
19. Pinacho-Castellanos, S. A., Garcia-Jacas, C. R., Gilson, M. K. & Brizuela, C. A. Alignment-free antimicrobial peptide predictors: improving performance by a thorough analysis of the largest available data set. *J. Chem. Inf. Model* **61**, 3141–3157 (2021).
20. Li, C. et al. AMPlify: attentive deep learning model for discovery of novel antimicrobial peptides effective against WHO priority pathogens. *BMC Genomics* **23**, 77 (2022).
21. de la Lastra, J. M. P., Wardell, S. J. T., Pal, T., de la Fuente-Nunez, C. & Pletzer, D. From data to decisions: leveraging artificial intelligence and machine learning in combating antimicrobial resistance—a comprehensive review. *J. Med. Syst.* **48**, 71 (2024).
22. Santos-Junior, C. D. et al. Discovery of antimicrobial peptides in the global microbiome with machine learning. *Cell* **187**, 3761–3778.e3716 (2024).
23. Cesaro, A. et al. Synthetic antibiotic derived from sequences encrypted in a protein from human plasma. *ACS Nano* **16**, 1880–1895 (2022).
24. Mishra, B. et al. Antimicrobial peptide developed with machine learning sequence optimization targets drug resistant *Staphylococcus aureus* in mice. *J. Clin. Invest.* https://doi.org/10.1172/JCI185430 (2025).
25. Yoshida, M. et al. Using evolutionary algorithms and machine learning to explore sequence space for the discovery of antimicrobial peptides. *Chem.-Us* **4**, 533–543 (2018).
26. Zhang, H. et al. Machine learning and genetic algorithm-guided directed evolution for the development of antimicrobial peptides. *J. Adv. Res.* https://doi.org/10.1016/j.jare.2024.02.016 (2024).
27. Xia, X., Torres, M. D. T. & de la Fuente-Nunez, C. Proteasome-derived antimicrobial peptides discovered via deep learning. Preprint at *bioRxiv* https://doi.org/10.1101/2025.03.17.643752 (2025).
28. Wan, F., Torres, M. D. T., Guan, C. & de la Fuente-Nunez, C. Tutorial: guidelines for the use of machine learning methods to mine genomes and proteomes for antibiotic discovery. *Nat. Protoc.* **20**, 2685–2697 (2025).
29. Porto, W. F., Pires, A. S. & Franco, O. L. CS-AMPPred: an updated SVM model for antimicrobial activity prediction in cysteine-stabilized peptides. *PLoS One* **7**, e51444 (2012).
30. Kim, W. et al. A new class of synthetic retinoid antibiotics effective against bacterial persisters. *Nature* **556**, 103–107 (2018).
31. Umetani, M. et al. Observation of persister cell histories reveals diverse modes of survival in antibiotic persistence. *Elife* **14**, e79517 (2025).
32. Luro, S., Potvin-Trottier, L., Okumus, B. & Paulsson, J. Isolating live cells after high-throughput, long-term, time-lapse microscopy. *Nat. Methods* **17**, 93–100 (2020).
33. Conlon, B. P. et al. Activated ClpP kills persisters and eradicates a chronic biofilm infection. *Nature* **503**, 365–370 (2013).
34. Nishi, H., Komatsuzawa, H., Fujiwara, T., McCallum, N. & Sugai, M. Reduced content of lysyl-phosphatidylglycerol in the cytoplasmic membrane affects susceptibility to moenomycin, as well as vancomycin, gentamicin, and antimicrobial peptides, in *Staphylococcus aureus*. *Antimicrob. Agents Chemother.* **48**, 4800–4807 (2004).
35. Green, B. N. et al. Methicillin-resistant *Staphylococcus aureus*: an overview for manual therapists(). *J. Chiropr. Med.* **11**, 64–76 (2012).
36. Souli, M. et al. Changing characteristics of *Staphylococcus aureus* bacteremia: results from a 21-year, prospective, longitudinal study. *Clin. Infect. Dis.* **69**, 1868–1877 (2019).
37. CDC. *Centers for Disease Control and Prevention*. *Vital Signs* https://www.cdc.gov/vitalsigns/staph/index.html (2019).
38. Lewis, K. Riddle of biofilm resistance. *Antimicrob. Agents Chemother.* **45**, 999–1007 (2001).
39. Liu, C. et al. Clinical practice guidelines by the Infectious Diseases Society of America for the treatment of methicillin-resistant *Staphylococcus aureus* infections in adults and children: executive summary. *Clin. Infect. Dis.* **52**, 285–292 (2011).
40. Wan, F. & de la Fuente-Nunez, C. Mining for antimicrobial peptides in sequence space. *Nat. Biomed. Eng.* **7**, 707–708 (2023).
41. Huang, J. et al. Identification of potent antimicrobial peptides via a machine-learning pipeline that mines the entire space of peptide sequences. *Nat. Biomed. Eng.* **7**, 797–810 (2023).
42. Maasch, J., Torres, M. D. T., Melo, M. C. R. & de la Fuente-Nunez, C. Molecular de-extinction of ancient antimicrobial peptides enabled by machine learning. *Cell Host Microbe* **31**, 1260–1274 e1266 (2023).
43. Torres, M. D. T. et al. Mining for encrypted peptide antibiotics in the human proteome. *Nat. Biomed. Eng.* **6**, 67–75 (2022).
44. Hurdle, J. G., O'Neill, A. J., Chopra, I. & Lee, R. E. Targeting bacterial membrane function: an underexploited mechanism for treating persistent infections. *Nat. Rev. Microbiol.* **9**, 62–75 (2011).
45. Blondelle, S. E. & Houghten, R. A. Design of model amphipathic peptides having potent antimicrobial activities. *Biochemistry* **31**, 12688–12694 (1992).
46. Zhang, S. K. et al. Design of an alpha-helical antimicrobial peptide with improved cell-selective and potent anti-biofilm activity. *Sci. Rep.* **6**, 27394 (2016).
47. Silva, O. N. et al. Repurposing a peptide toxin from wasp venom into antiinfectives with dual antimicrobial and immunomodulatory properties. *Proc. Natl. Acad. Sci. USA* **117**, 26936–26945 (2020).
48. Mwangi, J., Kamau, P. M., Thuku, R. C. & Lai, R. Design methods for antimicrobial peptides with improved performance. *Zool. Res.* **44**, 1095–1114 (2023).
49. Lakshmaiah Narayana, J. et al. Two distinct amphipathic peptide antibiotics with systemic efficacy. *Proc. Natl. Acad. Sci. USA* **117**, 19446–19454 (2020).
50. Wang, G. et al. Transformation of human cathelicidin LL-37 into selective, stable, and potent antimicrobial compounds. *ACS Chem. Biol.* **9**, 1997–2002 (2014).
51. Mishra, B. et al. Sequence permutation generates peptides with different antimicrobial and antibiofilm activities. *Pharmaceuticals* **13**, 271 (2020).
52. Rios, T. B. et al. Anti-staphy peptides rationally designed from Cry10Aa bacterial protein. *ACS Omega* **9**, 29159–29174 (2024).
53. Brogden, K. A. Antimicrobial peptides: pore formers or metabolic inhibitors in bacteria. *Nat. Rev. Microbiol.* **3**, 238–250 (2005).
54. Lee, M. T., Chen, F. Y. & Huang, H. W. Energetics of pore formation induced by membrane active peptides. *Biochemistry* **43**, 3590–3599 (2004).
55. Juba, M. L. et al. Helical cationic antimicrobial peptide length and its impact on membrane disruption. *Biochim. Biophys. Acta* **1848**, 1081–1091 (2015).
56. Shi, J., Chen, C., Wang, D., Wang, Z. & Liu, Y. The antimicrobial peptide LI14 combats multidrug-resistant bacterial infections. *Commun. Biol.* **5**, 926 (2022).
57. Ye, Z. et al. Synergistic collaboration between AMPs and non-direct antimicrobial cationic peptides. *Nat. Commun.* **15**, 7319 (2024).
58. Gomari, M. M. et al. Peptidomimetics in cancer targeting. *Mol. Med.* **28**, 146 (2022).
59. Mishra, B., Lakshmaiah Narayana, J., Lushnikova, T., Wang, X. & Wang, G. Low cationicity is important for systemic in vivo efficacy of database-derived peptides against drug-resistant Gram-positive pathogens. *Proc. Natl. Acad. Sci. USA* **116**, 13517–13522 (2019).

60. Goormaghtigh, F. & Van Melderen, L. Single-cell imaging and characterization of *Escherichia coli* persister cells to ofloxacin in exponential cultures. *Sci. Adv.* **5**, eaav9462 (2019).
61. Truong-Bolduc, Q. C. et al. *Staphylococcus aureus* AbcA transporter enhances persister formation under beta-lactam exposure. *Antimicrob. Agents Chemother.* **68**, e0134023 (2024).
62. Thomas, R. E. & Thomas, B. C. Reducing biofilm infections in burn patients' wounds and biofilms on surfaces in hospitals, medical facilities and medical equipment to improve burn care: a systematic review. *Int. J. Environ. Res. Public Health* **18**, 13195 (2021).
63. Claeys, K. C. et al. Acute bacterial skin and skin structure infections treated with intravenous antibiotics in the emergency department or observational unit: experience at the detroit medical center. *Infect. Dis. Ther.* **4**, 173–186 (2015).
64. Branski, L. K. et al. Emerging infections in burns. *Surg. Infect.* **10**, 389–397 (2009).
65. Koziel, J. & Potempa, J. Protease-armed bacteria in the skin. *Cell Tissue Res.* **351**, 325–337 (2013).
66. Wang, C. et al. Evolution of resistance mechanisms and biological characteristics of rifampicin-resistant *Staphylococcus aureus* strains selected in vitro. *BMC Microbiol.* **19**, 220 (2019).
67. Zhu, X. et al. Nigericin is effective against multidrug resistant gram-positive bacteria, persisters, and biofilms. *Front. Cell Infect. Microbiol.* **12**, 1055929 (2022).
68. Pirtskhalava, M. et al. DBAASP v3: database of antimicrobial/cytotoxic activity and structure of peptides as a resource for development of new therapeutics. *Nucleic Acids Res.* **49**, D288–D297 (2021).
69. Determination of minimum inhibitory concentrations (MICs) of antibacterial agents by broth dilution. *Clin. Microbiol. Infect.* **9**, ix-xv (2003).
70. Landrum, G. *RDKit: Open-source Cheminformatics* https://www.rdkit.org (2023).
71. Cock, P. J. et al. Biopython: freely available Python tools for computational molecular biology and bioinformatics. *Bioinformatics* **25**, 1422–1423 (2009).
72. Stokes, J. M. et al. A deep learning approach to antibiotic discovery. *Cell* **180**, 688–702 e613 (2020).
73. Hall, L. H. & Kier, L. B. in *Reviews in Computational Chemistry Reviews in Computational Chemistry*, Vol. **21**, 367–422 (Wiley, 1991).
74. Morgan, H. L. The generation of a unique machine description for chemical structures-a technique developed at chemical abstracts service. *J. Chem. Doc.* **5**, 107–113 (2002).
75. Elnaggar, A. et al. ProtTrans: toward understanding the language of life through self-supervised learning. *IEEE Trans. Pattern Anal. Mach. Intell.* **44**, 7112–7127 (2022).
76. Breiman, L. Random forests. *Mach. Learn.* **45**, 5–32 (2001).
77. Chen, T. & Guestrin, C. in *Proc 22nd ACM SIGKDD International Conference on Knowledge Discovery and Data Mining* 785–794 (ACM, 2016).
78. Kim, S.-J., Koh, K., Lustig, M., Boyd, S. & Gorinevsky, D. An interior-point method for large-scale-regularized least squares. *IEEE J. Sel. Top. Signal Process.* **1**, 606–617 (2007).
79. Klaproth-Andrade, D. et al. Deep learning-driven fragment ion series classification enables highly precise and sensitive de novo peptide sequencing. *Nat. Commun.* **15**, 151 (2024).
80. Rücker, C., Rücker, G. & Meringer, M. y-Randomization and its variants in QSPR/QSAR. *J. Chem. Inf. Modeling* **47**, 2345–2357 (2007).
81. Dathe, M. & Wieprecht, T. Structural features of helical antimicrobial peptides: their potential to modulate activity on model membranes and biological cells. *Biochim. Biophys. Acta* **1462**, 71–87 (1999).
82. Li, J., Hu, S., Jian, W., Xie, C. & Yang, X. Plant antimicrobial peptides: structures, functions, and applications. *Bot. Stud.* **62**, 5 (2021).
83. Wang, G., Li, X. & Wang, Z. APD3: the antimicrobial peptide database as a tool for research and education. *Nucleic Acids Res.* **44**, D1087–D1093 (2016).
84. de Santana, C. J. C., Pires Junior, O. R., Fontes, W., Palma, M. S. & Castro, M. S. Mastoparans: a group of multifunctional alpha-helical peptides with promising therapeutic properties. *Front. Mol. Biosci.* **9**, 824989 (2022).
85. Hori, Y. et al. Interaction of mastoparan with membranes studied by 1H-NMR spectroscopy in detergent micelles and by solid-state 2H-NMR and 15N-NMR spectroscopy in oriented lipid bilayers. *Eur. J. Biochem.* **268**, 302–309 (2001).
86. Sahu, C., Jain, V., Mishra, P. & Prasad, K. N. Clinical and laboratory standards institute versus European Committee for antimicrobial susceptibility testing guidelines for interpretation of carbapenem antimicrobial susceptibility results for *Escherichia coli* in urinary tract infection (UTI). *J. Lab Physicians* **10**, 289–293 (2018).
87. Felix, L., Mishra, B., Khader, R., Ganesan, N. & Mylonakis, E. In vitro and in vivo bactericidal and antibiofilm efficacy of alpha mangostin against *Staphylococcus aureus* persister cells. *Front. Cell Infect. Microbiol.* **12**, 898794 (2022).
88. Kim, W. et al. Identification of an antimicrobial agent effective against methicillin-resistant *Staphylococcus aureus* persisters using a fluorescence-based screening strategy. *PLoS One* **10**, e0127640 (2015).
89. Mishra, B. et al. Design and evaluation of short bovine lactoferrin-derived antimicrobial peptides against multidrug-resistant *Enterococcus faecium*. *Antibiotics* **11**, 1085 (2022).
90. Peng, J., Mishra, B., Khader, R., Felix, L. & Mylonakis, E. Novel cecropin-4 derived peptides against methicillin-resistant *Staphylococcus aureus*. *Antibiotics* **10**, 36 (2021).
91. Mishra, B. et al. Site specific immobilization of a potent antimicrobial peptide onto silicone catheters: evaluation against urinary tract infection pathogens. *J. Mater. Chem. B* **2**, 1706–1716 (2014).
92. Sani, M. A., Rajput, S., Keizer, D. W. & Separovic, F. NMR techniques for investigating antimicrobial peptides in model membranes and bacterial cells. *Methods* **224**, 10–20 (2024).
93. Crusca, E. Jr. et al. NMR structures and molecular dynamics simulation of hylin-a1 peptide analogs interacting with micelles. *J. Pept. Sci.* **23**, 421–430 (2017).
94. Shen, Y., Delaglio, F., Cornilescu, G. & Bax, A. TALOS + : a hybrid method for predicting protein backbone torsion angles from NMR chemical shifts. *J. Biomol. NMR* **44**, 213–223 (2009).
95. Guntert, P. Automated NMR structure calculation with CYANA. *Methods Mol. Biol.* **278**, 353–378 (2004).
96. Jumper, J. et al. Highly accurate protein structure prediction with AlphaFold. *Nature* **596**, 583–589 (2021).
97. Kumar, A., Mishra, B., Konar, A. D., Mylonakis, E. & Basu, A. Molecular dynamics simulations help determine the molecular mechanisms of lasioglossin-III and its variant peptides' membrane interfacial interactions. *J. Phys. Chem. B* **128**, 6049–6058 (2024).
98. Jo, S., Kim, T., Iyer, V. G. & Im, W. CHARMM-GUI: a web-based graphical user interface for CHARMM. *J. Comput. Chem.* **29**, 1859–1865 (2008).
99. Humphrey, W., Dalke, A. & Schulten, K. VMD: visual molecular dynamics. *J. Mol. Graph* **14**, 27–38 (1996).
100. Epand, R. M. & Epand, R. F. Lipid domains in bacterial membranes and the action of antimicrobial agents. *Biochim. Biophys. Acta* **1788**, 289–294 (2009).

101. Kim, S. M. et al. Antimicrobial activity of the membrane-active compound nTZDpa is enhanced at low pH. *Biomed. Pharmacother.* **150**, 112977 (2022).
102. Mishra, B. et al. A novel antimicrobial peptide derived from modified N-terminal domain of bovine lactoferrin: design, synthesis, activity against multidrug-resistant bacteria and Candida. *Biochim. Biophys. Acta* **1828**, 677–686 (2013).
103. Sherman, M. B. et al. Near-atomic-resolution cryo-electron microscopy structures of cucumber leaf spot virus and red clover necrotic mosaic virus: evolutionary divergence at the icosahedral three-fold axes. *J. Virol.* **94**, e01439-19 (2020).
104. Fey, P. D. et al. A genetic resource for rapid and comprehensive phenotype screening of nonessential *Staphylococcus aureus* genes. *mBio* **4**, e00537–00512 (2013).
105. Novogene. *Sequencing Platform* https://www.novogene.com/us-en/technology/platforms/ (2025).
106. Oscorbin, I. P. & Filipenko, M. L. M-MuLV reverse transcriptase: Selected properties and improved mutants. *Comput. Struct. Biotechnol. J.* **19**, 6315–6327 (2021).
107. Ling, L. L. et al. A new antibiotic kills pathogens without detectable resistance. *Nature* **517**, 455–459 (2015).
108. McDonald, P. J., Craig, W. A. & Kunin, C. M. Persistent effect of antibiotics on *Staphylococcus aureus* after exposure for limited periods of time. *J. Infect. Dis.* **135**, 217–223 (1977).
109. Haukland, H. H. & Vorland, L. H. Post-antibiotic effect of the antimicrobial peptide lactoferricin on *Escherichia coli* and *Staphylococcus aureus*. *J. Antimicrob. Chemother.* **48**, 569–571 (2001).
110. de Breij, A. et al. The antimicrobial peptide SAAP-148 combats drug-resistant bacteria and biofilms. *Sci. Transl. Med.* **10**, eaan4044 (2018).
111. The Cytokine Core. *Sample Handling: Collection, Storage, Shipping, and Submission* https://www.multiplex-cytokine-analysis.com/sample-collection-storage-shipping-and-submission/ (2025).
112. Love, M. I., Huber, W. & Anders, S. Moderated estimation of fold change and dispersion for RNA-seq data with DESeq2. *Genome Biol.* **15**, 550 (2014).

Acknowledgements

The authors gratefully acknowledge Michelle C. Swick, PhD, ELS, and Rachael Whitehead, MS (Academic Affairs, Houston Methodist Academic Institute) for scientific editing and illustration support. They also thank Jianhua Gu (Electron Microscopy Core) and Dr. Aijun Zhang, MD, MS (Department of Medicine) at Houston Methodist Academic Institute, for their assistance with microscopy, and Decha Pinkaew, PhD, for assistance with the gel electrophoresis. This work was supported by the P01AI083214 grant to EM. This work was also supported by the National Institutes of Health under institutional development award P20GM121344 from the National Institute of General Medical Sciences, which funds the COBRE, Center for AMR and Therapeutic Discovery to EM and a project leader grant to BM at the Department of Medicine, The Miriam Hospital, Warren Alpert Medical School of Brown University, Providence, Rhode Island, USA. The funders had no role in the study's design, data collection or analysis, preparation of the manuscript, or the decision to publish.

Author contributions

Conceived and designed the experiments: F.S., B.M., and E.M. Performed the experiments: F.S., B.M., R.F.-E., A.B., L.O., N.G., M.T.N., C.D., L.Z., and M.B.S. Analyzed the data: F.S., B.M., R.F.-E., L.O., A.B., J.P., M.B.S., M.T.N., P.P.S, and E.M. Contributed reagents/materials/analysis tools: F.S., B.M., A.B., J.P., M.T.N., M.B.S., A.M., Y.G., E.M. Writing—original draft: F.S., B.M., R.F.-E., A.B., M.T.N., and E.M. Writing—review and editing: F.S., B.M., A.B., J.P., M.T.N., M.B.S., P.P.S, E.M. All authors have read and agreed to publish the current version of the manuscript.

Competing interests

The authors declare no competing interests.

Declaration of generative AI and AI-assisted technologies in the writing process

During the preparation of this work, the authors used ChatGPT for language editing in order to improve readability. After using this service, the authors reviewed and edited the content as needed and take full responsibility for the content of the published article.

Additional information

Supplementary information The online version contains supplementary material available at https://doi.org/10.1038/s41467-026-70348-9.

Correspondence and requests for materials should be addressed to Eleftherios Mylonakis.

Peer review information *Nature Communications* thanks Amir Pandi, and the other, anonymous, reviewer(s) for their contribution to the peer review of this work. A peer review file is available.

Reprints and permissions information is available at http://www.nature.com/reprints

Publisher's note Springer Nature remains neutral with regard to jurisdictional claims in published maps and institutional affiliations.

Open Access This article is licensed under a Creative Commons Attribution-NonCommercial-NoDerivatives 4.0 International License, which permits any non-commercial use, sharing, distribution and reproduction in any medium or format, as long as you give appropriate credit to the original author(s) and the source, provide a link to the Creative Commons licence, and indicate if you modified the licensed material. You do not have permission under this licence to share adapted material derived from this article or parts of it. The images or other third party material in this article are included in the article's Creative Commons licence, unless indicated otherwise in a credit line to the material. If material is not included in the article's Creative Commons licence and your intended use is not permitted by statutory regulation or exceeds the permitted use, you will need to obtain permission directly from the copyright holder. To view a copy of this licence, visit http://creativecommons.org/licenses/by-nc-nd/4.0/.

© The Author(s) 2026